Chemical Engineering Journal 540 (2026) 177494

Contents lists available at ScienceDirect

Chemical Engineering Journal

journal homepage: www.elsevier.com/locate/cej

Reliability enhancement of PVDF-HFP modified perovskite solar cells under synergistic space-relevant stress conditions

Harini Srikanth Rao [a], Seoungjun Ahn [a], Wei-Hao Chiu [b], Wei-Chen Chu [a], Yi-Wen Sung [a], Gao Chen [c], Kun-Mu Lee [a,b,d,e,*]

[a] Department of Chemical and Materials Engineering, Chang Gung University, Taoyuan, 33302, Taiwan
[b] Center for Sustainability and Energy Technologies, Chang Gung University, Taoyuan, 33302, Taiwan
[c] Department of Applied Physics, The Hong Kong Polytechnic University, Hung Hom Kowloon, Hong Kong, 999077, PR China
[d] Division of Neonatology, Department of Pediatrics, Chang Gung Memorial Hospital, Linkou, Taoyuan, 33305, Taiwan
[e] College of Environment and Resources, Ming Chi University of Technology, New Taipei City, 24301, Taiwan

ARTICLE INFO

Keywords:
Perovskite solar cell
Space application
Thermal stress
Polymer-modified

ABSTRACT

Thermal stress represents a critical reliability bottleneck for perovskite solar cells (PSCs) in space environments, where sustained high temperatures can accelerate irreversible degradation. Beyond isolated thermal effects, PSCs in orbit experience synergistic stressors including vacuum, illumination, and elevated temperature. This study investigates the stability of p-i-n PSCs under combined vacuum + light (V + L) and vacuum + heat (V + H) conditions, focusing on thermally activated interfacial failure and polymer-based mitigation. Devices are evaluated under two temperature regimes: moderate (85 and 100 °C) and extreme (115 and 130 °C) V + H stress, together with prolonged V + L exposure. The results show that degradation is dominated by interface-driven non-radiative recombination rather than bulk absorber failure, with ΔV_3 increase, QFLS reduction, and interface-specific pseudo-PCE loss, identifying the perovskite/PCBM as the primary weak point under V + H stress. Incorporation of poly(vinylidene fluoride-*co*-hexafluoropropylene) (PVDF-HFP) into the perovskite layer effectively suppresses defect generation, preserves microstructural integrity, and improves charge-extraction stability, leading to enhanced performance retention. Hazard-based Weibull-Arrhenius analysis confirms extended characteristic lifetimes for PVDF-HFP devices at moderate temperatures, with a higher activation energy (0.95 eV vs 0.83 eV) indicating a modified degradation pathway. Room-temperature lifetime is further predicted using a graphical extrapolation method, yielding significantly extended projected operational lifetimes for polymer-modified devices. These findings establish a reliability enhancement of the PVDF-HFP-modified devices under synergetic space-relevant stress.

1. Introduction

Space exploration has entered an era of sustained activity, spanning low Earth orbit (LEO), cislunar infrastructure, and deep-space missions with increasingly long operational lifetimes [1]. In this context, perovskite solar cells (PSCs) have emerged as promising candidates due to their high power-to-weight ratio, strong optical absorption in thin films, and bandgap tunability that enables flexible device architectures [2]. However, the space environment is uniquely harsh, combining high vacuum, energetic particle radiation, ultraviolet exposure, reactive atomic oxygen, and repeated thermal cycling. In LEO alone, components can experience temperature excursions from approximately −100 °C to +130 °C, imposing severe thermo-mechanical stress, interfacial fatigue, and accelerated diffusion-driven degradation [3]. These coupled stressors can progressively alter electrical, optical, and mechanical properties in ways not captured by standard terrestrial protocols, and because many systems are inaccessible after deployment, even gradual degradation can cascade into functional failure at the device or system level. Consequently, establishing materials and interfaces that maintain stable performance under combined thermal, radiative, and vacuum stress is essential for reliable, long-duration deployment of PSC technologies in space [4–6].

Polymers are increasingly viewed as enabling materials for durable photovoltaic (PV) stacks because they can simultaneously tune film

* Corresponding author at: Department of Chemical and Materials Engineering, Chang Gung University, Taoyuan, 33302, Taiwan.
E-mail address: KMLee@mail.cgu.edu.tw (K.-M. Lee).

https://doi.org/10.1016/j.cej.2026.177494
Received 16 March 2026; Received in revised form 1 May 2026; Accepted 17 May 2026
Available online 18 May 2026

formation, interfaces, and long-term stability. In PSCs, polymers are attractive compared with small molecules and inorganic additives because they offer multifunctional chemical groups, high thermal stability, flexible long chains, and cross-linking capability, allowing multiple stabilization mechanisms to operate at once [7]. Through controlled polymer-perovskite interactions, polymers can regulate crystallization kinetics to improve film uniformity and reduce defect density, which supports carrier transport and reduces non-radiative recombination losses [8–12]. Polymers can also suppress degradation pathways linked to ionic motion: the review highlights that perovskites have a soft ionic lattice and low defect formation energy, making them susceptible to heat/light-induced ionic defects and field-assisted ion migration; polymer barriers and passivation can mitigate these effects [13–16]. Beyond internal modification, polymer encapsulation is emphasized as a stability lever, with desired encapsulant properties including resistance to heat, oxygen, and ultraviolet radiation, compatibility in thermal expansion to avoid delamination, and low-temperature processing to avoid damaging perovskites. Collectively, these attributes make polymer engineering a practical route to improving device reliability under demanding operating conditions [7].

Poly(vinylidene fluoride-*co*-hexafluoropropylene) (PVDF-HFP) is a fluorinated copolymer that has been introduced as a polymer additive in PSCs to improve film quality and operational durability under harsh environments. Prior studies show that incorporating PVDF-HFP can retard perovskite crystallization and guide more uniform film formation, yielding improved optoelectronic quality and enhanced device performance [17]. Further reports show that PVDF-HFP additives promote larger perovskite grains and reduce grain-boundary related losses, which benefits charge transport and stabilizes photovoltaic operation over time [18]. In addition to these benefits, the fluorinated nature of PVDF-HFP is particularly relevant for space-oriented PSCs. Fluorinated polymers generally exhibit strong chemical and thermal stability associated with C—F bonding, and they have also been reported to show lower atomic-oxygen erosion susceptibility in low-Earth-orbit environments [19]. These characteristics make PVDF-HFP a relevant material platform for chemically aggressive and thermally demanding space conditions.

In our previous study, we evaluated PVDF-HFP-modified PSCs under space-relevant stressors, specifically high vacuum and gamma-ray irradiation [20]. Under high vacuum exposure, pristine devices showed performance decay consistent with vacuum-accelerated degradation of the perovskite stack. In contrast, PVDF-HFP-modified devices maintained substantially higher operational stability over prolonged testing. Under gamma-ray irradiation, the PVDF-HFP-modified devices exhibited improved resilience, with the observed performance drop tracking the reduction in substrate transmittance more closely than intrinsic degradation of the PV stack [20]. Together, these results support PVDF-HFP as a practical additive strategy for improving perovskite device robustness under vacuum and radiation conditions relevant to space operation.

Thermal cycling and high-temperature exposure are widely used accelerated-stress protocols for assessing the operational robustness of PSCs, because both stressors can perturb charge extraction and recombination pathways in ways not captured under room-temperature testing. Temperature-dependent impedance trends reinforce this interpretation: increasing temperature is associated with higher charge-transfer resistance and lower recombination resistance, indicating increasingly inefficient interfacial carrier extraction alongside enhanced recombination [21]. At the materials level, perovskite exhibits lattice expansion with temperature and a tetragonal-to-cubic transition near ~55 °C, coinciding with a performance drop and sensitivity to thermal-expansion mismatch at the charge transport layer (CTL)/perovskite interface [22]. Under sustained operation up to ~80 °C the hole transport layer (HTL) can become a dominant weak link, with doped spiroOMeTAD showing more severe and irreversible degradation, consistent with temperature-sensitive additive loss [23]. Taken together, these findings indicate that high-temperature stress primarily accelerates interfacial/transport degradation and non-radiative recombination, providing direct motivation for this study's focus on improving thermal reliability under space-relevant operation.

This study examines the reliability of p-i-n PSCs under space-relevant stress conditions, aiming to identify thermally activated failure pathways and assess polymer-enabled stabilization. Unlike our previous work, which primarily focused on material-level stabilization of n-i-p devices, this study introduces a combined-stressor framework by systematically integrating low vacuum, continuous illumination, and elevated thermal stress to probe the degradation mechanism under realistic operating conditions. The present study is designed primarily to investigate degradation pathways and reliability enhancement under combined space-relevant stress conditions rather than to optimize champion photovoltaic performance. By combining low vacuum exposure, illumination, and elevated thermal stress across moderate (85 and 100 °C) and extreme (115 and 130 °C) regimes, degradation is found to be dominated by interface-driven non-radiative recombination. V_{oc} loss-component analysis and optoelectronic measurements indicate that the perovskite/PCBM junction is the most thermally vulnerable interface. Incorporation of PVDF-HFP within the perovskite absorber suppresses defect growth, improves morphological retention, and enhances charge-extraction stability, leading to improved performance retention and longer characteristic lifetimes at moderate high temperatures. A hazard-based lifetime analysis is used to quantify temperature-dependent durability, showing extended characteristic lifetimes for PVDF-HFP devices at moderate high temperatures. Weibull-Arrhenius modeling indicates a higher activation energy for PVDF-HFP devices, reflecting a modified degradation pathway. Room-temperature lifetime is further predicted using a graphical extrapolation method, confirming a reliability advantage for polymer-modified devices. Overall, this study not only demonstrates polymer-enabled stabilization but also establishes its operational limits under space-relevant conditions.

2. Results and discussion

This study systematically examines the structural, morphological, optical, electronic, and photovoltaic responses of p-i-n perovskite solar cells under operational thermal-stability stressors and continuous illumination, along with controlled vacuum. Throughout, perovskite films/devices containing PVDF-HFP are referred to as “PVDF-HFP film/device,” and those without the additive as “pristine film/device”. Fig. 1a illustrates the PVDF-HFP/perovskite interactions established in our previous study [20]. The fluorine atoms in PVDF-HFP are reported to interact with the perovskite through hydrogen-bonding interactions with MA^+/FA^+ and Lewis-base coordination with under-coordinated Pb^{2+} at surfaces/grain boundaries. Such N-H···F interactions have been inferred in prior studies from the ^1H nuclear magnetic resonance (NMR) chemical shift of the -NH_3^+ proton upon incorporation of fluorinated polymers such as PVDF and PVDF-HFP into the perovskite system [24]. These interactions retard crystallization, stabilize phase/texture, and bridge grain boundaries, thereby suppressing non-radiative recombination. The selection of PVDF-HFP is based on its ability to improve perovskite film and device stability through defect passivation and grain boundary stabilization [24,25]. In addition, the selection of PVDF-HFP was motivated by the need to evaluate its thermal stability limits under elevated temperature conditions, as its behavior in PSCs under high-temperature stress has not been systematically studied.

Throughout this work, vacuum exposure ($\approx 10^{-3}$ Torr) is employed as a consistent stress condition to mimic the low-pressure space environment (i.e., near-atmosphere-free operation), enabling a direct comparison of material and device stability. Although this pressure is higher than LEO ($\sim 10^{-7}$ Torr), NASA-TM-20250004276 reports that a chamber pressure of $\sim 10^{-3}$ Torr is sufficient to ensure minimal heat transfer through the surrounding gas, thereby approximating vacuum-dominated conditions [26]. To further validate this for PSCs, the PCE

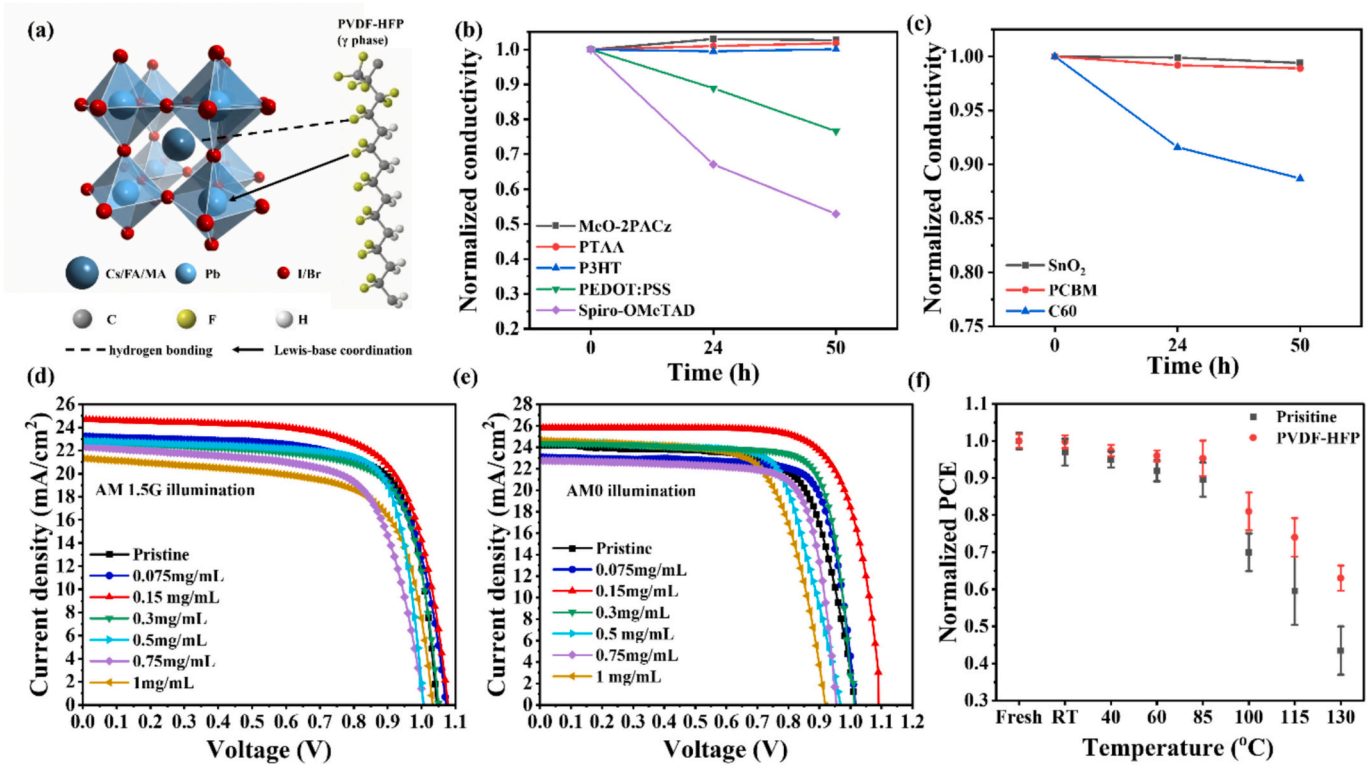

Fig. 1. Overview of interfacial interactions and device-level effects associated with PVDF-HFP incorporation. (a) Schematic illustration demonstrating the interactions between the perovskite absorber and PVDF-HFP. (b) Normalized conductivity evolution of various HTLs under vacuum +100 °C stress for 50 h. (c) Normalized conductivity evolution of different ETLs under the same conditions. J-V characteristics of devices incorporating different PVDF-HFP concentrations measured under (d) AM 1.5G illumination, (e) AM 0 illumination. (f) Normalized PCE as a function of temperature for pristine and PVDF-HFP devices measured over 100 h, highlighting their comparative thermal stability.

was measured before and after 300 h across a wide pressure range (760 Torr to 10^{-7} Torr) for the encapsulated devices, as shown in Fig. S1. This revealed negligible variation with vacuum level, indicating that device degradation is largely insensitive to further pressure reduction, supporting the use of $\approx 10^{-3}$ Torr as a practical proxy for space-relevant conditions.

Meanwhile, to evaluate the intrinsic thermal stability of charge-transport layers, various p-type and n-type thin films were spin-coated on fluorine-doped tin oxide (FTO) substrates, followed by Ag top-electrode deposition to form vertical test structures for conductivity measurements. The samples were subjected to combined vacuum and thermal stress at 100 °C, and the conductivity was monitored as a function of exposure time. The resulting trends for p-type and n-type layers are summarized in Fig. 1b and c, respectively. For the p-layer (Fig. 1b), 2-(9H-carbazol-9-yl)ethylphosphonic acid (MeO-2PACz) showed the highest conductivity retention, likely because its dopant-free self-assembled monolayer (SAM) structure forms an ultrathin, chemically anchored interface with fewer mobile species, reducing diffusion and improving interfacial stability compared with conventional bulk HTL [27]. For the n-layer (Fig. 1c), SnO_2 was identified as the most stable material, aligning with its widespread use as a robust electron transport layer (ETL) in n-i-p perovskite devices. Among p-i-n device stacks, [6,6]-Phenyl-C_{61}-butyric acid methyl ester (PCBM) exhibited better stability than C_{60} under the same thermal stress. Along with these stability comparisons, multiple ETL/passivation combinations were screened in pristine devices. The corresponding J-V curves are shown in Fig. S2, and the extracted PV parameters are summarized in Table S1. The PCBM/PEI stack delivered the best overall device performance and was therefore selected as the ETL/passivation layer for subsequent device fabrication.

To assess concentration effects in the perovskite, PVDF-HFP was added at 0.075, 0.15, 0.3, 0.5, 0.75 or 1 mg/mL in the perovskite solution. The corresponding J-V responses of PVDF-HFP devices, alongside the pristine devices, are presented in Fig. 1d (AM 1.5 illumination). The J-V responses highlight a strong dependence on PVDF-HFP concentration. Among all devices, the 0.15 mg/mL PVDF-HFP device achieved superior performance, with higher short-circuit current density (J_{sc}) and open-circuit voltage (V_{oc}) than both the pristine and other additive concentrations. Devices with concentrations below or above this optimum show less pronounced improvement, while higher PVDF-HFP concentrations lead to a gradual reduction in performance. Overall, these results indicate that 0.15 mg/mL is the optimal PVDF-HFP concentration for achieving improved device performance. Fig. 1e shows the J-V responses of pristine and PVDF-HFP-modified devices under AM0 illumination. Unlike AM 1.5G, the AM0 spectrum represents unattenuated sunlight with a broader distribution and stronger ultraviolet contribution [28]. The concentration-dependent trend under AM0 mirrors the AM 1.5G results, with the 0.15 mg/mL PVDF-HFP device outperforming all other concentrations and the pristine device. However, all devices achieve higher absolute metrics under AM0, as the spectrum provides about 22% more photon flux relative to AM 1.5G [29]. At a lower concentration (0.075 mg/mL), the polymer concentration is likely insufficient to regulate crystallization or provide substantial defect-passivation effectively, resulting in device behavior similar to that of the pristine case. The superior performance of the 0.15 mg/mL PVDF-HFP devices under both AM0 and AM 1.5G suggests that this concentration strikes the optimal balance between stabilization and charge transport. At this level, PVDF-HFP contributes to mechanical strengthening and interfacial passivation but does not interfere with crystallization or conductivity. As Wang et al. note, excessive polymer incorporation can lead to phase separation, non-uniform morphology, and reduced carrier mobility, which become evident at 0.5 and 1 mg/

mL, resulting in poorer photovoltaic performance [7].

To determine mechanistically meaningful stress temperatures for long-term stability evaluation, preliminary accelerated aging experiments were conducted across a wide temperature range for 100 h (Fig. 1f). The normalized power conversion efficiency (PCE) exhibits a clear nonlinear temperature dependence, with a distinct change in the degradation slope near 85 °C, indicating the presence of a dominant degradation pathway. Beyond ~85 °C, a pronounced decline in normalized PCE is observed, indicating the onset of significant thermal stress on device performance. To systematically explore temperature-driven degradation under vacuum and heat, a set of representative stress temperatures was selected. Accordingly, V + H stability tests were conducted at 85 °C, 100 °C, 115 °C, and 130 °C to evaluate device durability under progressively stronger thermal stress.

In this study, before proceeding to high-temperature thermal stability tests, the light stability of the devices under 1 sun illumination in vacuum was first evaluated. To distinguish the contribution of illumination from vacuum alone, device stability under vacuum-only conditions was evaluated as a baseline (Fig. S1). The observed degradation under combined vacuum and light conditions is not solely attributable to vacuum exposure, indicating that illumination plays a dominant role in driving the degradation. Illumination inevitably leads to device heating, with 1 sun exposure increasing the temperature to approximately ~45–50 °C. Fig. 2 shows the device stability under combined vacuum + light (V + L) along with the structural and optoelectronic changes in the perovskite films. Fig. 2a shows that encapsulated pristine devices fall below 80% of their initial PCE at ~900 h and retain 74.6% at 1000 h. In contrast, encapsulated PVDF-HFP devices retain 85.1% after 1000 h, demonstrating improved operational stability. The corresponding change in V_{oc}, J_{sc} and fill factor (*FF*) over time is given in Fig. S3. The stability of unencapsulated devices was also evaluated under the same V + L conditions (Fig. S4): at 1000 h, unencapsulated pristine devices degrade to 29.1%, while unencapsulated PVDF-HFP devices retain 67.0%, confirming that PVDF-HFP enhances stability even without encapsulation (although encapsulation remains essential for long-term retention).

The V_{oc} loss was analyzed to understand the contribution of various factors to the loss of V_{oc} of the PSCs under V + L conditions. To quantify the origin of V_{oc} losses, the total voltage loss (ΔV) was defined as [30]:

$$q\Delta V = E_g - qV_{oc} \tag{1}$$

This total loss can be further decomposed into three physically distinct contributions:

$$q\Delta V = \left(E_g - qV_{oc}^{SQ}\right) + \left(qV_{oc}^{SQ} - qV_{oc}^{rad}\right) + \left(qV_{oc}^{rad} - qV_{oc}\right) \tag{2}$$

$$q\Delta V = q(\Delta V_1 + \Delta V_2 + \Delta V_3) \tag{3}$$

Here, q is the elementary charge, E_g is the bandgap energy of the absorber, and V_{oc} is the experimentally measured open circuit voltage. V_{oc}^{SQ} denotes the Shockley-Queisser limit corresponding to the maximum achievable V_{oc} under ideal conditions, while V_{oc}^{rad} represents the open-circuit voltage assuming only radiative recombination. Accordingly, ΔV_1 corresponds to the thermodynamic loss, ΔV_2 represents radiative recombination loss, and ΔV_3 accounts for non-radiative recombination loss. These V_{oc} loss measurements are presented in Fig. 2b, and the corresponding values are given in Table S2. Before 500 h of V + L exposure, the ΔV_1 values for both pristine and PVDF-HFP devices were 0.272 V, which remained the same after the exposure. The unchanged ΔV_1 suggests that the absorber energetic limit is largely preserved, and that the observed V_{oc} degradation is dominated by recombination-related losses rather than changes in the fundamental bandgap limit. ΔV_2 occurs when photoexcited charge carriers (electrons and holes) recombine, making it closely related to the quality of the perovskite films. Both pristine and PVDF-HFP devices exhibited negligible changes in ΔV_2 value following the V + L exposure. These marginal fluctuations confirm that an increase in radiative recombination loss is not the

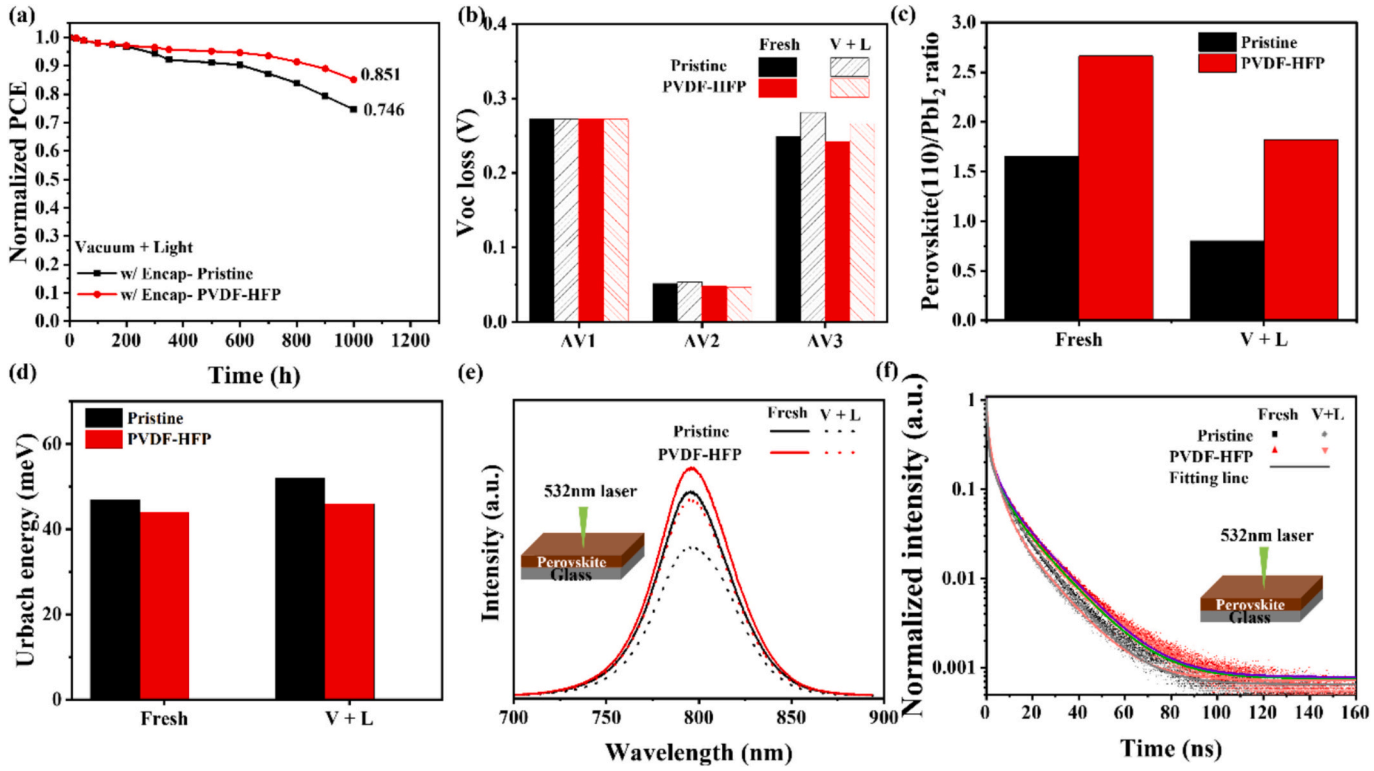

Fig. 2. Device- and film-level stability of pristine and PVDF-HFP systems under V + L stress. (a) Normalized PCE evolution of encapsulated devices with aging time. (b) V_{OC} loss before and after 500 h of V + L stress. Film-level changes under the same conditions are shown in (c–f): (c) perovskite (110)/PbI_2 peak-intensity ratio extracted from XRD, (d) Urbach energy derived from UV–Vis spectra, (e) PL spectra, and (f) TRPL decay curves for both pristine and PVDF-HFP films.

primary cause of the PCE reduction, pointing instead to non-radiative pathways as the dominant factor. ΔV_3 occurs when charge carriers recombine without emitting a photon, typically associated with bulk defects and buried interfaces. For pristine devices, ΔV_3 increased from 0.249 V to 0.281 V, while for the PVDF-HFP devices, the increase is less pronounced, going from 0.242 V to 0.266 V. These results indicate that the increase in non-radiative recombination is an important reason for the PCE reduction, which is substantially reduced by the addition of PVDF-HFP [25].

The smaller increase in ΔV_3 suggests that PVDF-HFP slows the development of illumination-induced recombination pathways during V + L aging. This stabilizing effect is attributed to fluorine-mediated interactions between PVDF-HFP and the perovskite, including N-H···F interactions with organic cations and coordination with undercoordinated Pb^{2+} sites. These interactions can passivate defect-prone sites and stabilize the perovskite, thereby reducing the formation or activation of non-radiative recombination centers under continuous V + L [20,24,31].

To determine whether this improvement is associated with suppressed phase degradation, the perovskite/PbI_2 ratio was quantified from the X-ray diffraction (XRD) patterns (Fig. S5) and summarized in Fig. 2c. The fresh PVDF-HFP films exhibit a higher perovskite/PbI_2 ratio (~2.5) than pristine films, consistent with improved phase purity and/or a lower PbI_2 fraction. This initial difference is consistent with a fluorine-rich additive environment promoting a more phase-pure starting film, as fluorine-containing polymer systems have been shown to coordinate with perovskite species and suppress undesired intermediate/secondary phases during crystallization, thereby favoring more homogeneous film formation. The perovskite/PbI_2 ratio decreases after 500 h of V + L for both films (Fig. S5; Fig. 2c), indicating PbI_2 formation during vacuum light soaking. However, the reduction is substantially larger in pristine films, while PVDF-HFP maintains a higher ratio, consistent with the polymer delaying light-driven phase degradation and PbI_2 accumulation. Such behavior aligns with fluorine-containing polymer approaches that combine coordination-assisted defect suppression with improved film uniformity, which can mitigate photo-activated ionic/defect pathways that can contribute to phase decomposition under continuous illumination [32].

To further investigate the trap states and gain a deeper understanding of the optoelectronic properties of the fabricated perovskite films, an analysis was conducted involving Urbach energy (E_u), photoluminescence (PL), and time-resolved photoluminescence (TRPL). E_u is a key parameter that reflects the material's crystallinity, defect density, and overall optoelectronic performance. The UV–Vis spectra and ln (absorption coefficient) vs energy plots are shown in Fig. S6, and E_u values obtained from them are summarized in Fig. 2d. Fresh PVDF-HFP films show a lower Urbach energy than pristine films (44 meV and 47 meV, respectively), indicating a lower initial degree of band-tailing. This reflects a reduced density of shallow band-tail states, likely due to suppressed electronic disorder arising from reduced photo-induced halide fluctuation even before aging. As shown in Table S3, after 500 h V + L, the pristine film shows a pronounced increase from 47 meV to 52 meV ($\Delta E_u = 5$ meV), whereas the PVDF-HFP film increases only from 44 meV to 46 meV ($\Delta E_u = 2$ meV). Under V + L conditions, disorder accumulation is dominated by illumination-induced defect activation rather than lattice damage, and the smaller increase in E_u for PVDF-HFP indicates slower generation of photo-active sub-gap states [33]. The smaller net increase in Urbach energy for PVDF-HFP supports the V_{oc}-loss analysis, indicating that fluorine-mediated passivation slows the growth of defect-associated band-tail states that contribute to ΔV_3 under V + L stress.

Steady-state PL spectra (Fig. 2e) decrease in intensity after V + L aging for both films, consistent with a higher contribution of non-radiative recombination following prolonged illumination. This reduction in PL can be interpreted as an increase in recombination pathways associated with illumination-exposed films, such as the activation of recombination-active defects or sub-gap states. Notably, the PVDF-HFP films retain a higher PL intensity than the pristine films after aging, suggesting a comparatively lower degree of recombination degradation. Time-resolved PL results (Fig. 2f and Table S3) support this trend: the average lifetime decreases from 18.04 to 14.70 ns for pristine films after 500 h V + L, whereas PVDF-HFP shows a smaller reduction from 20.22 to 18.23 ns. The stronger PL/TRPL retention further shows that PVDF-HFP preserves carrier lifetime by limiting the buildup of defect-assisted recombination pathways during V + L aging.

To evaluate whether V + L aging induces surface roughening or morphological damage that can promote interfacial recombination and accelerate degradation, atomic force microscopy (AFM) was used to quantify nanoscale topography changes in the perovskite films. The AFM results shown in Fig. 3 indicate that the pristine film exhibits an increase in RMS roughness from 24.3 nm to 30.9 nm after 500 h of V + L exposure, reflecting pronounced surface/morphology evolution. In contrast, the PVDF-HFP film shows only a modest change in root mean square (RMS) roughness from 22.9 nm to 23.7 nm over the same treatment, indicating that PVDF-HFP better preserves the film morphology and suppresses stress-induced roughening. This improved morphological retention is consistent with the scanning electron microscopy (SEM) observations provided in Fig. S7. Such morphological changes are commonly associated with variations in film uniformity, grain boundary structure, and surface coverage, as reported in previous studies on perovskite films [34]. In this context, the suppressed roughness evolution in PVDF-HFP films indicates improved morphological stability under V + L stress, suggesting a more uniform and structurally intact film compared to the pristine counterpart.

Vacuum illumination imposes photo-thermal stress, evidenced by lattice shrinkage and morphological deformation, while photo-generated carriers facilitate ion migration and interfacial reactions. This condition therefore captures space-relevant, photo-thermally assisted degradation and provides a practical baseline before isolating purely thermal effects in dark high-temperature tests. Under V + L aging, the dominant signature is an increase in non-radiative V_{oc} loss (ΔV_3), consistent with illumination-activated defects and field-assisted ion redistribution, and supported by PL quenching, shortened TRPL lifetimes, and a slight Urbach-energy rise. Pristine films further show reduced perovskite/PbI_2 ratio and increased roughness, indicating concurrent structural/morphological evolution. In contrast, PVDF-HFP mitigates the illumination-induced growth of recombination-active defects, leading to a slower increase in ΔV_3. This suppression is consistent with reduced activation of defect-mediated non-radiative pathways

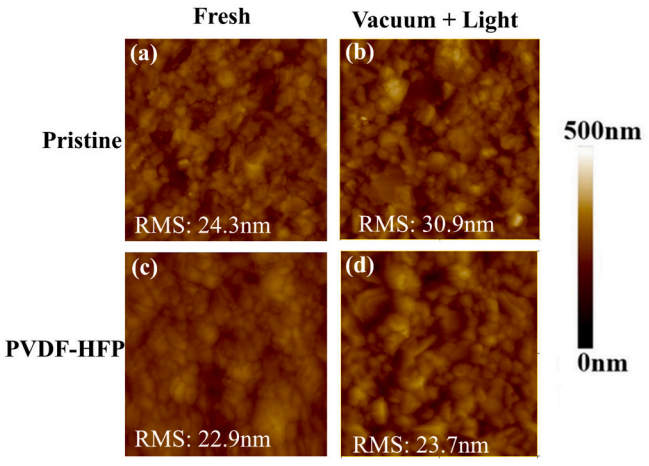

Fig. 3. AFM images of perovskite films under vacuum + light (V + L) conditions. (a) Fresh pristine film, (b) pristine film after V + L stress, (c) fresh PVDF-HFP film, and (d) PVDF-HFP film after V + L stress, enabling comparison of surface morphology evolution.

under illumination, rather than changes in the intrinsic energetic limit or radiative recombination [35]. Overall, PVDF-HFP mitigates these changes, showing smaller ΔV_3, better perovskite/PbI_2 and PL/TRPL retention, minimal Urbach-energy increase, and suppressed roughening, indicating that polymer incorporation limits the photo-thermally assisted generation of non-radiative recombination centers, thereby explaining the improved PCE retention under V + L exposure.

Following the evaluation of the stability of pristine and PVDF-HFP films and devices under V + L stress, thermal stability was subsequently investigated at high temperatures. As detailed above, temperatures of 85 °C, 100 °C, 115 °C and 130 °C were selected to represent accelerated thermal stress conditions, enabling a systematic assessment of temperature-induced stability of both pristine and PVDF-HFP devices. Fig. 4 summarizes the thermal stability of 16 devices under vacuum at these temperatures. Fig. 4a shows the normalized PCE of these devices over time. Across all temperature conditions, the incorporation of PVDF-HFP improves device stability by slowing the progression of degradation, as reflected by the consistently extended lifetimes compared to pristine devices. In Fig. 4a, at 85 °C, the PVDF-HFP devices maintain a high normalized PCE close to unity for most of the time and still retain 0.794 at ~1200 h, whereas pristine devices show a steady decline across aging, ending at 0.637. Consistent with this trend, the T_{80} (time required to reach 80% of the initial PCE) increases from ~900 h for pristine devices to ~1200 h for PVDF-HFP devices. At 100 °C, pristine devices degrade continuously and reach failure much earlier, while the PVDF-HFP devices degrade more gradually, remaining near ~0.9 for several hundred hours, and still retaining 0.431 at ~1000 h. The corresponding T_{80} lifetimes increase from ~150 h for pristine devices to ~500 h with PVDF-HFP incorporation, indicating a substantial improvement in thermal durability. When the temperature is increased to 115 °C, degradation accelerates for both device types; however, the PVDF-HFP devices continue to show improved stability, with T_{80} extending from ~100 h for pristine devices to ~200 h for PVDF-HFP devices. Under the most severe condition of 130 °C, rapid performance loss occurs within the first several tens of hours for both devices, yet the PVDF-HFP devices still maintain a modest advantage, with T_{80} increasing from ~40 h in pristine devices to ~50 h in PVDF-HFP devices. Both device types were aged until failure to enable subsequent reliability analysis, and further characterization was performed to identify the dominant degradation pathways responsible for device failure.

Based on this mechanistic separation, two distinct temperature regimes were defined for subsequent accelerated stability experiments. The 85 °C and 100 °C conditions were grouped as moderate high-temperature stress, representing the regime where degradation begins to accelerate but devices still retain measurable operational lifetimes (T_{80} on the order of hundreds of hours). In this range, degradation processes are expected to involve a combination of interfacial instability, ionic redistribution, and the early stages of MA-related chemical degradation, enabling meaningful comparison of stability trends and mechanistic differences between pristine and PVDF-HFP modified devices [36].

In contrast, 115 °C and 130 °C were treated as extreme thermal stress regimes, in which degradation becomes strongly chemically driven and proceeds much more rapidly. Under these conditions, the operational lifetimes collapse to tens to a few hundred hours, indicating the onset of accelerated perovskite decomposition and thermally activated interfacial failure processes. Separating these temperatures into distinct regimes, therefore, allows evaluation of device stability under severe stress conditions, provides insight into the intrinsic limits of material and interface stability, and enables comparison of how PVDF-HFP modification influences device robustness when chemical degradation pathways dominate [37–39].

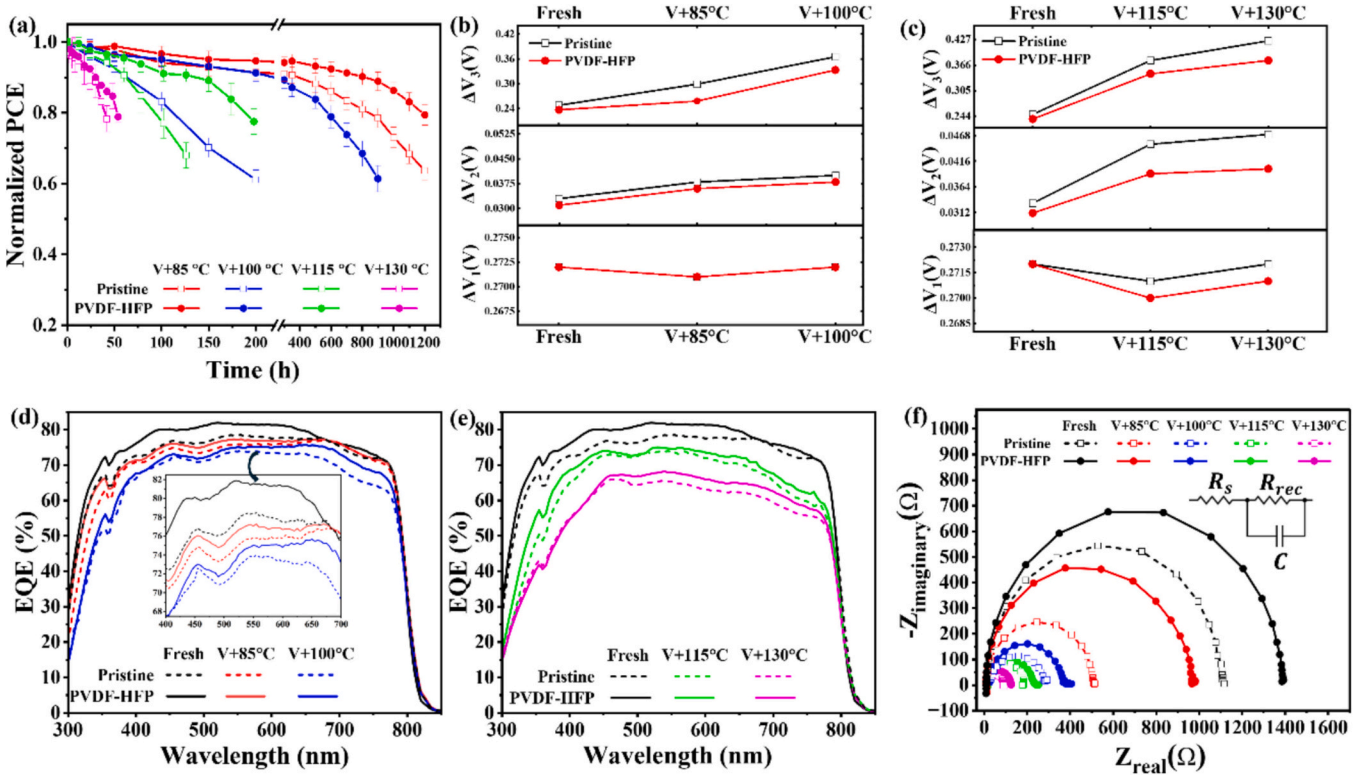

Fig. 4. Device-level stability of pristine and PVDF-HFP devices under vacuum + thermal stress. (a) Normalized PCE evolution of encapsulated devices with aging time, (b) V_{OC} loss before and after 500 h of V + 85 °C and V + 100 °C, (c) V_{OC} loss before and after 50 h of V + 115 °C and V + 130 °C. (d) EQE of pristine and PVDF-HFP devices after V + 85 °C and V + 100 °C aging, (e) EQE of pristine and PVDF-HFP devices after V + 115 °C and V + 130 °C aging, (f) Nyquist plots of pristine and PVDF-HFP devices measured under LED illumination at 0 V bias before and after one week of vacuum + heat (V + H) exposure at 85, 100, 115, and 130 °C. The inset shows the equivalent circuit used to analyze the impedance response.

The rapid failure at 130 °C is consistent with PVDF-HFP approaching its thermally activated softening regime [40]. Differential scanning calorimetry (DSC) analysis in Fig. S8 shows a distinct endothermic melting peak at 157 °C during heating, while the cooling scan exhibits a crystallization peak at 127 °C, confirming a semicrystalline nature of the polymer. Importantly, the heating curve reveals that the heat flow begins to increase noticeably after 135 °C, indicating the onset of melting and progressive disruption of crystalline domains prior to the peak temperature. As the polymer enters this transition regime, its structural rigidity is reduced, weakening its ability to maintain effective defect passivation and interfacial stabilization. This provides a direct explanation for the observed narrowing of the performance gap between pristine and PVDF-HFP devices at 130 °C. While PVDF-HFP enhances stability at moderate temperatures, its passivation capability diminishes as the material approaches the onset of melting, leading to accelerated device failure under high thermal stress.

In this temperature window, PVDF-HFP has been reported to undergo pronounced, and in some cases irreversible, structural reorganization (e.g., crystal phase changes) even below complete melting, implying reduced stability of polymer-derived structural functionality near 120–130 °C. Accordingly, the stabilizing effect of PVDF-HFP within polymer-modified microstructures may diminish at elevated temperature, potentially weakening grain-boundary and interfacial stabilization. Such thermal activation could facilitate local morphological rearrangement and exacerbate interfacial degradation pathways, thereby accelerating performance loss and leading to rapid device failure at 130 °C [41]. Fig. S9 presents the corresponding aging results under V + 85 °C and V + 100 °C for unencapsulated devices. At 85 °C, the pristine devices drop below 80% of their initial PCE within ~200 h, whereas the PVDF-HFP devices maintain comparable performance until ~600 h. At 100 °C, degradation is markedly faster for both device types, with the normalized PCE decreasing to ~0.14 for pristine devices and ~0.435 for PVDF-HFP devices within ~150 h. In comparison with the encapsulated devices, these results clearly demonstrate that encapsulation significantly improves device stability, and its stabilizing effect is particularly evident under high-temperature stress. Because degradation accelerates strongly at higher temperatures, unencapsulated tests were not performed at 115 °C and 130 °C. Encapsulated devices already show short lifetimes at these temperatures (T_{80} ≈ 100 h at 115 °C and ≈ 40 h at 130 °C for pristine devices), and degradation would be expected to proceed even faster without encapsulation. Therefore, unencapsulated measurements were limited to 85 °C and 100 °C, where meaningful stability comparisons can be obtained.

Because two distinct temperature regimes were defined, the duration of the stability tests was selected based on the highest-temperature T_{80} of the PVDF-HFP devices within each regime. For the 85–100 °C regime, the stability tests were performed before and after 500 h of aging, corresponding to the T_{80} of the PVDF-HFP devices at 100 °C. For the 115–130 °C extreme thermal stress regime, the stability tests were conducted before and after 50 h, corresponding to the T_{80} of the PVDF-HFP devices at 130 °C. This approach enables consistent comparison while probing device behavior near the characteristic degradation limit within each regime.

Fig. 4b and Table S4 show a loss-component analysis of the V_{oc} degradation under V + 85 °C and V + 100 °C after 500 h of aging. The thermodynamic term (ΔV_1) is identical for pristine and PVDF-HFP devices before aging (0.272 V) and remains essentially unchanged after both V + 85 °C and V + 100 °C treatments, indicating that the observed V_{oc} decay is not governed by changes in the bandgap-related thermodynamic limit. In contrast, the radiative loss contribution (ΔV_2) increases after heat exposure, with a larger rise in the pristine devices (0.033 → 0.038 at 85 °C and 0.040 at 100 °C) than in the PVDF-HFP devices (0.031 → 0.036 at 85 °C and 0.038 at 100 °C), suggesting that PVDF-HFP partially mitigates the aging-induced increase in radiative losses. The most pronounced change occurs in the non-radiative recombination loss term (ΔV_3), which increases from 0.248 V (fresh) to 0.299 V after V + 85 °C and further to 0.365 V after V + 100 °C for pristine devices. In comparison, PVDF-HFP devices start from a slightly lower ΔV_3 (0.237 V) and exhibit a smaller increase to 0.258 V (V + 85 °C) and 0.333 V (V + 100 °C), indicating reduced non-radiative recombination during thermal aging [42].

To further identify the degradation pathway under extreme thermal stress, the same V_{oc} loss analysis was performed for devices measured before and after 50 h of V + heat at 115 °C and 130 °C (Fig. 4c and Table S5). Similar to the moderate temperature regime, ΔV_1 remains nearly constant for both device types (≈0.27 V), and ΔV_2 increases only slightly (pristine: 0.033 → 0.045 (115 °C) → 0.047 V (130 °C); PVDF-HFP: 0.031 V → 0.039 V → 0.040 V), confirming that these components are not dominant contributors to degradation. Instead, the primary change is a strong increase in ΔV_3, reflecting intensified non-radiative recombination. For pristine devices ΔV_3 rises from 0.248 V to 0.377 V at 115 °C and further to 0.424 V at 130 °C, while PVDF-HFP devices show a smaller increase from 0.237 V to 0.345 V and 0.377 V, respectively. The larger increase at 130 °C compared with 115 °C indicates more severe interfacial degradation at higher temperature, although PVDF-HFP partially suppresses this degradation pathway [20].

Fig. 4d and Fig. 4e show the evolution of the external quantum efficiency (EQE) spectra before and after thermal aging under V + heat conditions for the moderate (85 °C and 100 °C, 500 h) and extreme (115 °C and 130 °C, 50 h) temperature regimes, respectively. For both regimes, the pristine devices exhibit a clear reduction in EQE across the entire spectral range after thermal exposure, indicating a loss in charge collection efficiency. This decrease becomes more pronounced at higher temperatures, particularly under V + 130 °C, where the pristine device shows the strongest suppression of EQE. Such reductions in EQE are consistent with thermally induced degradation processes that increase recombination and reduce carrier extraction efficiency, including the interfacial degradation and partial perovskite decomposition. These effects reduce the probability that photogenerated carriers are successfully collected, leading to lower EQE values [43].

In contrast, the PVDF-HFP modified devices maintain consistently higher EQE after thermal aging across most of the wavelength range. The smaller reduction in EQE suggests that PVDF-HFP helps suppress thermally activated defect formation and mitigates interfacial recombination losses, thereby preserving carrier collection efficiency. This stabilizing effect is particularly evident at elevated temperatures, where the divergence between pristine and PVDF-HFP devices becomes more pronounced. The improved EQE retention in PVDF-HFP devices therefore indicates that the polymer additive contributes to maintaining absorber quality and interface integrity during thermal stress, consistent with the reduced non-radiative recombination losses observed in the V_{oc} loss analysis [18].

To further probe the electrical response after thermal aging, IS measurements were performed under LED illumination at 0 V bias, after one week of V + H exposure for all samples. The Nyquist spectra in Fig. 4f were fitted using an $R_s + (R_{rec} \parallel C)$ equivalent circuit, and the extracted fitting parameters are summarized in Table S6. With increasing aging temperature, the semicircle diameter decreases for both pristine and PVDF-HFP devices, indicating reduced R_{rec} and enhanced recombination after thermal stress. However, PVDF-HFP devices retain larger semicircle diameters and higher R_{rec} values than pristine devices under the same aging conditions, suggesting suppressed recombination and improved interfacial stability. At higher temperatures, particularly 115 and 130 °C, the slight low-frequency tail suggests the activation of slower interfacial/electrochemical processes, which may be associated with thermally enhanced ion-migration-related polarization [44,45].

After completing the device stability tests, film stability was subsequently investigated to further understand the material-level degradation behavior. Fig. 5(a-f) compares the morphological evolution of pristine and PVDF-HFP perovskite films after thermal exposure at V + 85 °C and 100 °C. In the SEM images, the pristine film shows clear

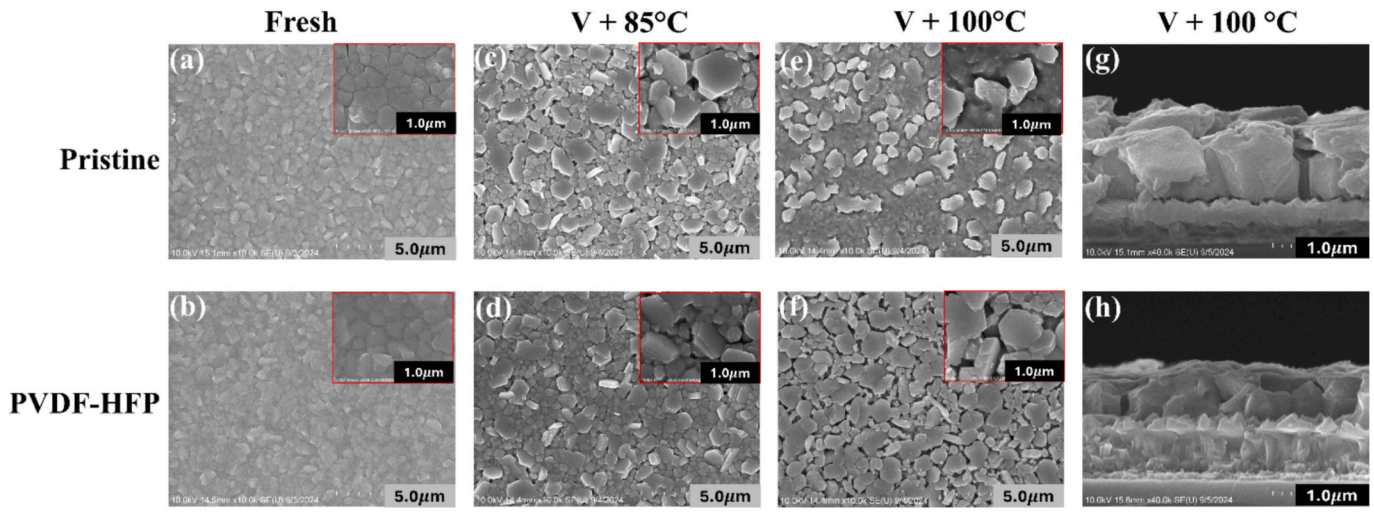

Fig. 5. Top-view and cross-sectional SEM images of perovskite films before and after 500 h of vacuum + thermal stress. Top-view images show (a) pristine fresh, (b) PVDF-HFP fresh, (c) pristine after V + 85 °C, (d) PVDF-HFP after V + 85 °C, (e) pristine after V + 100 °C, and (f) PVDF-HFP after V + 100 °C. Cross-sectional SEM images after V + 100 °C stress are shown in (g) pristine and (h) PVDF-HFP films.

degradation with temperature: at V + 85 °C, grain-boundary breakage becomes evident, while at V + 100 °C the film exhibits a pronounced increase in cracks together with widespread bright PbI_2 crystallites across the surface [46]. In contrast, the PVDF-HFP film remains comparatively more uniform at both temperatures; although some boundary breakage and minor cracking are visible (more apparent at V + 100 °C), the perovskite morphology is better retained than in the pristine case. This improved morphological retention is attributed to in-situ thermal crosslinking of the PVDF-HFP polymer during heat treatment. This leads to the formation of a polymer network that interacts with the perovskite and helps reduce defects. The crosslinked polymer helps stabilize the grain boundaries, as reported in prior studies [25]. It contributes to the formation of an interconnected polymer-perovskite microstructure that can help bind adjacent crystalline domains. Such a polymer-modified grain framework enhances the structural integrity of the film under thermal stress, thereby suppressing grain-boundary separation, crack propagation, and the development of severe surface discontinuities observed in the pristine film [47].

Consistent with the SEM trends, the AFM images in Fig. S10 show that surface roughness increases substantially with thermal exposure:

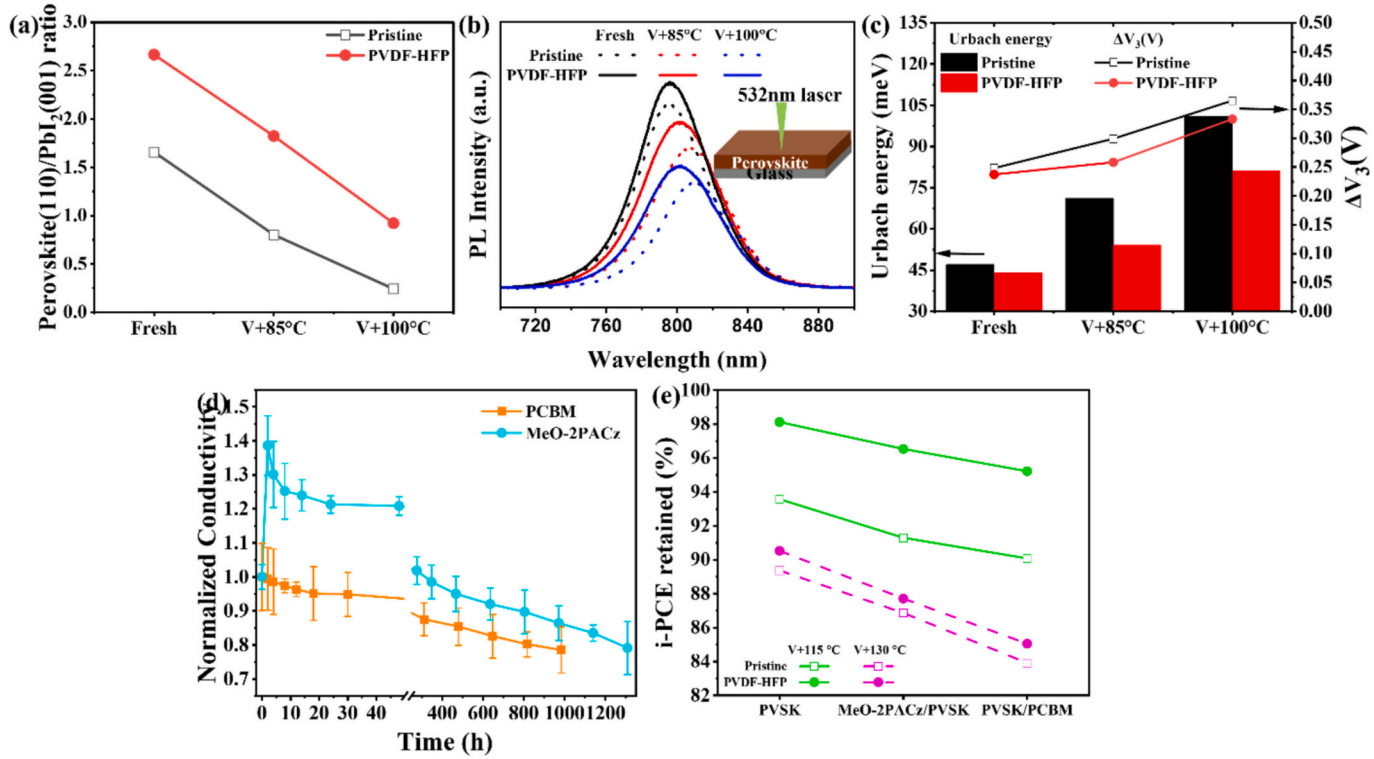

Fig. 6. Film-level stability of pristine and PVDF-HFP systems under vacuum + thermal stress (a) perovskite (110)/PbI_2 peak-intensity ratio extracted from XRD after aging at V + 85 °C and V + 100 °C, (b) PL intensity before and after aging at V + 85 °C and V + 100 °C (c) Urbach energy derived from UV–Vis spectra on the left and the ΔV_3 on the right for V + 85 °C and V + 100 °C, (c) Normalized conductivity evolution of 16 MeO-2PACz and 16 PCBM films under V + 130 °C and (e) Retained I–PCE response of PVSK, MeO-2PACz/PVSK, and PVSK/PCBM architectures after 50 h of V + 115 °C and V + 130 °C stress.

for the pristine film, RMS roughness rises from 24.3 nm (fresh) to 49.8 nm (V + 85 °C) and 66.0 nm (V + 100 °C), while the PVDF-HFP film increases from 22.9 nm (fresh) to 45.1 nm (V + 85 °C) and 65.1 nm (V + 100 °C), confirming pronounced roughening at higher temperature, with PVDF-HFP maintaining comparatively better morphological uniformity despite similar high-temperature roughness levels. Consistent with the morphological trends observed in the top-view SEM and AFM analyses, cross-sectional SEM images after V + 100 °C shown in Fig. 5g and h, reveal severe bulk degradation in the pristine perovskite film, characterized by pronounced vertical cracks, voids, and disrupted grain stacking across the film thickness. In contrast, the PVDF-HFP film maintains a compact and continuous cross-section with suppressed crack penetration and improved grain connectivity. This indicates that PVDF-HFP effectively mitigates thermally induced mechanical stress and mass transport along grain boundaries. The preserved through-thickness integrity confirms that PVDF-HFP enhances intrinsic absorber robustness under high-temperature bias stress.

To evaluate the thermal tolerance of pristine and PVDF-HFP films, changes in the crystal structure and chemical composition of the films were analyzed using XRD. As shown in Fig. 6a and Fig. S5, after 500 h, the ratio of perovskite to PbI_2 in the pristine film significantly decreased for V + 85 °C, and a more drastic decrease was seen for the films exposed to V + 100 °C. This reduction can be attributed to the stoichiometric imbalance caused by ammonium salts from the MA, which leads to the formation of the PbI_2 phase in pristine films under thermal stress [48]. In contrast, the PVDF-HFP film demonstrated greater stability, likely due to the strong bonding between fluorine and Pb^{2+}, which helps to maintain the structural integrity of the film [47].

PL measurements on both pristine and PVDF-HFP perovskite films, depicted in Fig. 6b, reveal a notably higher PL intensity in the PVDF-HFP film, suggesting better crystal quality. After 500 h at V + 85 °C and V + 100 °C, the emission peak showed a redshift. The PVDF-HFP film exhibited a moderate shift of 5.19 nm at V + 85 °C and 5.51 nm at V + 100 °C, whereas the pristine film showed a substantially larger shift of about 10.95 nm and 13.09 nm for V + 85 °C and V + 100 °C, respectively. This pronounced redshift in the pristine sample is attributed to an increased presence of PbI_2 at the grain boundaries at elevated temperatures [49]. Along with the redshift, the pristine film shows a substantial drop in the PL intensity. Compared with the pristine film, the PVDF-HFP film shows only a slight PL intensity loss after 500 h at both 85 and 100 °C, and the peak redshift is also smaller at each temperature. This behavior suggests that PVDF-HFP slows thermally driven defect formation and grain-boundary degradation (e.g., PbI_2 build-up), thereby better preserving radiative recombination and spectral stability [50].

TRPL decay measurements, displayed in Fig. S11, were performed on both pristine and PVDF-HFP films. The fitting parameters are summarized in Table 1. Bi-exponential TRPL analysis reveals clear differences in recombination dynamics between pristine and PVDF-HFP perovskite films under thermal stress. At 85 °C, the pristine film shows a pronounced reduction in both decay components after aging, with τ_1 decreasing from 8.29 to 6.46 ns and τ_2 from 21.37 to 18.35 ns, leading to a substantial drop in the average lifetime. In contrast, the PVDF-HFP film exhibits much smaller changes, with τ_1 remaining close to 9 ns and τ_2 preserved above 22 ns, indicating suppressed formation of fast non-radiative recombination pathways. A similar trend is observed at 100 °C: while the pristine film undergoes significant lifetime degradation (τ_1= 6.16 ns and τ_2 = 17.21 ns after aging), the PVDF-HFP film retains comparatively longer decay components (τ_1 = 7.15 ns and τ_2 = 19.37 ns). The consistently longer τ_2 and higher average lifetime in PVDF-HFP films at both temperatures indicate reduced trap-assisted recombination and better preservation of bulk electronic quality under thermal exposure.

Changes in electronic disorder were assessed via the Urbach energy extracted from UV–Vis spectra (Fig. S12 and S13) and plotted in Fig. 6c, since E_u reflects band-tail states and defect-related energetic disorder. The E_u for the pristine film is 47 meV, whereas the PVDF-HFP film exhibits a lower value of 44 meV, indicating reduced defect density in the latter. After 500 h of exposure at V + 85 and V + 100 °C, the E_u for the pristine film increased to 71 and 101 meV, respectively, while the PVDF-HFP film showed a smaller increase to 54 meV and 84 meV. As shown in Fig. 6c, the increase in Urbach energy closely follows the rise in ΔV_3, which is plotted together for comparison. This correlation indicates that the thermally induced increase in electronic disorder leads to enhanced non-radiative recombination, particularly at the interfaces. Therefore, the degradation observed in the devices is primarily associated with increased interfacial non-radiative recombination, while the PVDF-HFP films exhibit improved stability due to the smaller increase in both E_u and ΔV_3.

To further probe the intrinsic thermal robustness of the transport layers under the extreme thermal stress regime, the stability of MeO-2PACz and PCBM films was evaluated at V + 130 °C under V + heat conditions (Fig. 6d). Both layers show a gradual conductivity decay with time at 130 °C, consistent with accelerated thermal instability of the transport layers. For MeO-2PACz, a brief initial conductivity increase is observed, possibly arising from a high-temperature annealing effect before long-term degradation dominates. The subsequent MeO-2PACz failure is consistent with thermally induced SAM reorganization/desorption of weakly bound molecules, leading to non-uniform coverage and reduced hole transport [51]. In contrast, PCBM degrades more rapidly, consistent with heat-driven diffusion and aggregation/crystallization of fullerene domains, which is expected to reduce film uniformity and disrupt continuous electron percolation pathways, explaining the faster conductivity drop compared with the oxide-anchored MeO-2PACz SAM [52,53].

To pinpoint the interface(s) responsible for device failure, three simplified film stacks were examined: PVSK, MeO-2PACz/PVSK, and PVSK/PCBM. The pseudo-PCE (i-PCE) was extracted for all films before and after 50 h of V + heat stress at 115 °C and 130 °C, with the retained values summarized in Fig. 6e and Table S7. Across both temperatures, the bare PVSK film shows the highest i-PCE retention, whereas the introduction of charge-transport layers leads to enhanced degradation. In particular, PVSK/PCBM exhibits the strongest i-PCE loss, indicating that the PVSK/PCBM interface is the most thermally vulnerable, while MeO-2PACz/PVSK also contributes to degradation but to a lesser extent.

Importantly, PVDF-HFP consistently improves i-PCE retention for all film configurations at both temperatures. This mitigation is attributed to

Table 1
TRPL fitting parameters extracted from the TRPL decay curves shown in Fig. S11 and the E_u values for pristine and PVDF-HFP films before and after 500 h of vacuum + thermal stress at 85 °C and 100 °C.

Temperature	Sample		A_1	τ_1(ns)	A_2	τ_2(ns)	$\tau_{average}$(ns)	$E_u(meV)$	ΔE_u (meV)
85 °C	Pristine	Fresh	0.32	8.29	0.68	21.37	17.18	47	24
		After	0.41	6.46	0.58	18.35	13.29	71	
	PVDF-HFP	Fresh	0.31	8.38	0.69	24.38	19.42	44	10
		After	0.38	8.97	0.62	22.48	17.34	54	
100 °C	Pristine	Fresh	0.33	7.18	0.67	19.42	15.38	47	54
		After	0.42	6.16	0.58	17.21	12.86	101	
	PVDF-HFP	Fresh	0.31	8.25	0.59	23.48	18.75	44	40
		After	0.39	7.15	0.61	19.37	14.60	84	

PVDF-HFP's ability to passivate interfacial defects, suppress ion migration, and mechanically stabilize grain boundaries and interfaces, thereby reducing thermally activated non-radiative recombination and interfacial instability. The trend directly supports the conclusion that interface degradation, especially at the PVSK/PCBM junction, is the primary origin of extreme-temperature device failure, while polymer modification partially alleviates, but does not fully eliminate, this limitation.

The quasi-Fermi level splitting (QFLS) analysis provides evidence for interface-dependent degradation under vacuum + thermal stress. QFLS represents the maximum attainable internal photovoltage and is highly sensitive to non-radiative recombination; thus, a drop in QFLS indicates enhanced non-radiative recombination which is commonly associated with recombination-active defects at interfaces and within the absorber, including those linked to thermally activated ionic and structural disorder [54,55]. The spatial maps in Fig. 7a show that pristine stacks develop pronounced low-QFLS regions after stress, particularly for the CTL-containing architectures, whereas the PVDF-HFP-modified films in Fig. 7b retain improved spatial uniformity. The corresponding QFLS histograms (Fig. 7c–e) quantify these shifts. For the PVSK stack (Fig. 7c), pristine films decrease from 1.106 eV (fresh) to 1.048 eV at 115 °C and 1.031 eV at 130 °C, while PVDF-HFP films maintain higher values (1.13 → 1.113 → 1.107 eV), indicating strong suppression of thermally activated recombination pathways. The MeO-2PACz/PVSK architecture (Fig. 7d) exhibits a larger stress-induced loss in the pristine case (1.099 → 1.032 → 1.016 eV), consistent with increased interfacial recombination at the hole-extracting interface, whereas PVDF-HFP reduces the decline (1.114 → 1.085 → 1.074 eV). The most severe degradation occurs for the PVSK/PCBM stack (Fig. 7e), where pristine films drop to 0.998 eV at 130 °C from an initial 1.076 eV, reflecting substantial recombination at the electron-extracting interface. In contrast, PVDF-HFP-modified films retain 1.009 eV under the same condition, demonstrating partial mitigation of interface-driven defect formation. Overall, the downward histogram shifts confirm that degradation is strongly interface-governed, with the PVSK/PCBM junction being the most thermally vulnerable, and that PVDF-HFP incorporation suppresses defect generation and limits the activation of non-radiative recombination pathways across all stack configurations.

This result is consistent with the thermal instability of PCBM-based contacts reported by Huang et al. for triple-cation CsFAMA p-i-n devices [56]. In their study, CsFAMA/PCBM devices aged at 85 °C under N_2 showed rapid performance loss, mainly through V_{oc} reduction and

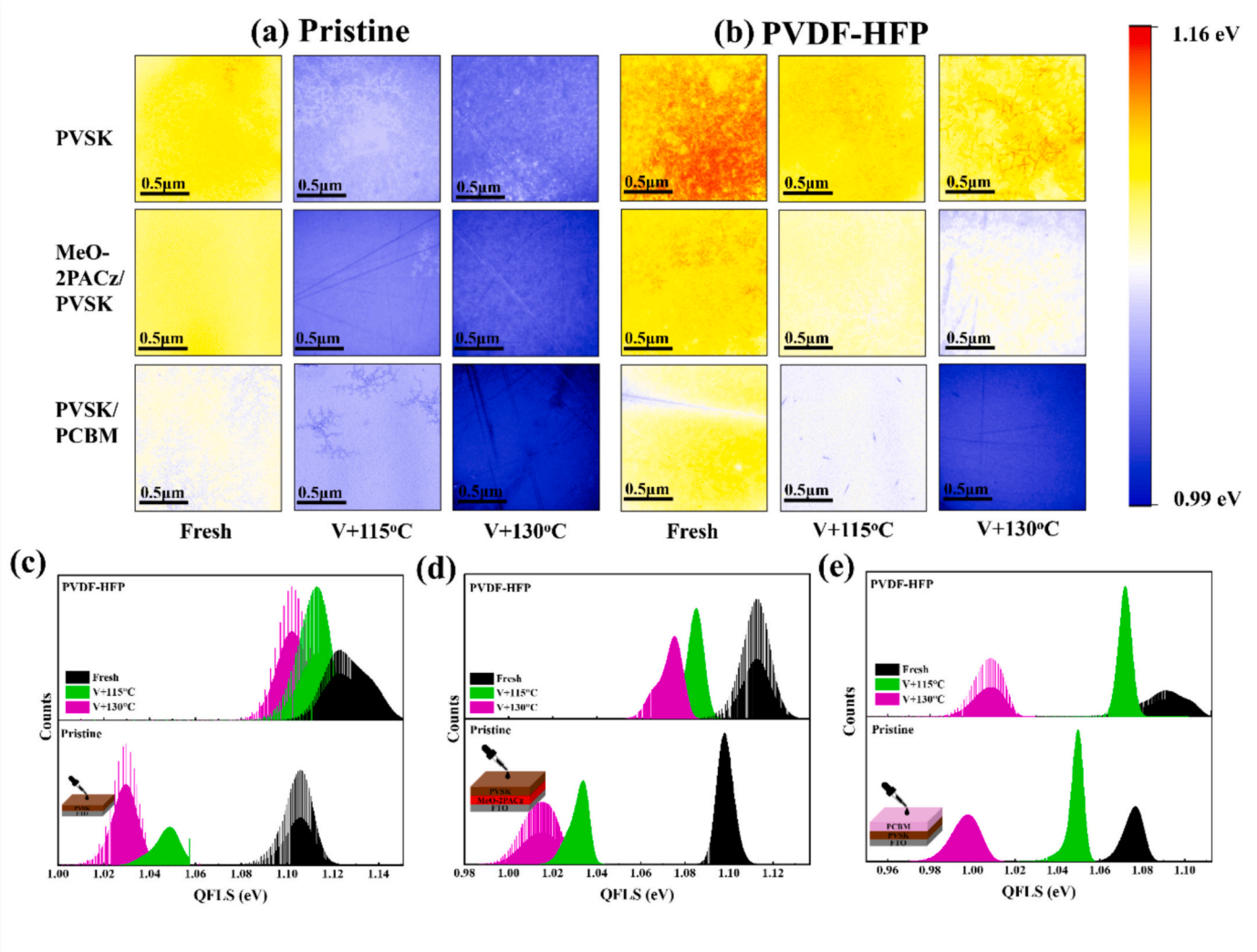

Fig. 7. Spatial quasi-Fermi level splitting (QFLS) maps and statistical distributions for pristine and PVDF-HFP-modified films under vacuum + thermal stress. Corresponding values are provided in Table S8. (a) QFLS maps of pristine PVSK, MeO-2PACz/PVSK, and PVSK/PCBM stacks after 50 h of combined vacuum and thermal stress (115 °C and 130 °C). (b) Corresponding QFLS maps of PVDF-HFP-modified films for the same stack architectures under identical stress conditions. Histograms of QFLS distributions extracted from the spatial maps for (c) PVSK, (d) MeO-2PACz/PVSK, and (e) PVSK/PCBM stacks, comparing pristine and PVDF-HFP films.

decreased shunt resistance, while J_{sc} remained comparatively stable, indicating recombination/leakage-dominated degradation rather than absorber-related optical loss. Huang et al. further showed that heat treatment at 65 °C for 600 h caused deformation and roughening of the PCBM layer, attributed to PCBM aggregation/crystallization, which increased carrier recombination and deteriorated R_{sh} and V_{oc}. In addition, Lee and Lee reported ion-diffusion-induced interfacial degradation in PCBM-based p-i-n devices, where iodide ions migrated from the perovskite toward the PCBM/Ag side and interacted with PCBM, introducing electronic disorder and recombination-active states that affect V_{oc}, FF, and QFLS. [57]. Therefore, when considered together with these literature reports, the simplified-stack i-PCE and QFLS measurements confirm that the PVSK/PCBM interface is the most vulnerable region under V + H conditions.

The improved stability of the PVSK/PCBM stack in the PVDF-HFP-modified films can be explained by a bulk-to-surface passivation pathway, consistent with previous PVDF-HFP and fluorinated-polymer reports [18,58,59]. Since PVDF-HFP is incorporated into the perovskite precursor, it can interact with grain-boundary regions and the terminal perovskite surface before PCBM deposition. In PVDF-HFP-based PSCs, the polar -CF_2- groups have been reported to coordinate with undercoordinated Pb^{2+} at perovskite surfaces and grain boundaries, reducing Pb-related defects and non-radiative recombination. Related fluorinated polymer systems also show that fluorine-mediated interactions with organic cation environments can regulate crystallization and stabilize the perovskite lattice. Therefore, the perovskite surface contacting PCBM becomes less recombination-active, even without forming a distinct PVDF-HFP interlayer. This interpretation is further supported by the impedance spectroscopy results, where the PVDF-HFP device retained higher R_{rec} than pristine devices, indicating suppressed recombination after thermal stress.

Based on the results presented above, across all tested temperatures, PVDF-HFP-modified devices consistently exhibit higher stability and performance retention than the pristine devices, confirming the beneficial role of polymer incorporation under thermal bias stress. Mechanistic analysis indicates that device failure is governed primarily by interfacial degradation, evidenced by the dominant increase in Δ V_3 and the concurrent losses in i-PCE/QFLS for interface-containing stacks. Among the interfaces, the PVSK/PCBM junction emerges as the most vulnerable, identifying the electron-extracting side as the key bottleneck under extreme high-temperature operation.

The next part quantifies device stability by extracting the characteristic lifetime of both pristine and PVDF-HFP devices. Lifetime metrics derived from stability results enable a direct comparison of degradation kinetics and provide a clear measure of how polymer incorporation improves durability under elevated-temperature operation. The characteristic lifetime was calculated using a hazard-based framework, where $h(t)$ denotes the hazard function (obtained by the ratio of devices failed to the number of working devices before failure), $H(t)$ the cumulative hazard function, and $F(t)$ is the failure probability at time t calculated using $F(t) = 1 - e^{-\left(\frac{t}{\eta}\right)^{\beta}}$ [60,61]. β and η are the Weibull parameters. β is the slope of the H(t) vs t curve, also called the shape parameter, and η is the characteristic lifetime at which H(t) becomes equal to 0.632. The corresponding calculations are summarized in Tables S9-S16. The H(t) vs time for pristine and PVDF-HFP are plotted in Fig. 8a and b, along with the Weibull parameters listed in the table inside the figure. The Weibull shape parameter (β) increases from 4.61 ± 0.39 for the pristine devices to 7.53 ± 0.70 for the PVDF-HFP modified devices. In Weibull reliability analysis, $\beta > 1$ corresponds to a wear-out dominated failure regime in which the failure rate increases with time due to progressive degradation. The higher β value for the PVDF-HFP devices therefore indicates a narrower failure distribution and reduced device-to-device variability, suggesting that the degradation process

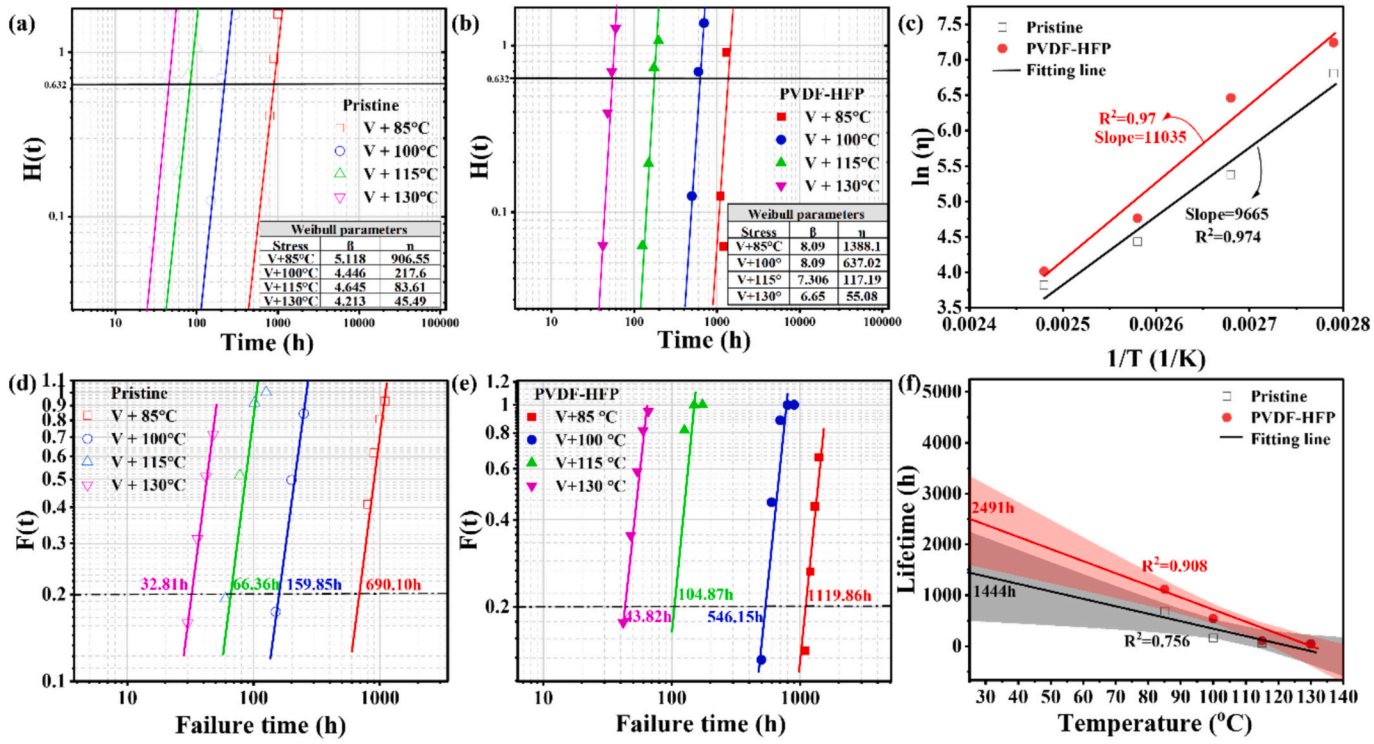

Fig. 8. Temperature-dependent reliability analysis under vacuum + thermal stress. (a) Cumulative hazard function, H(t) as a function of time for pristine devices at V + 85 °C, 100 °C, 115 °C, and 130 °C along with the Weibull parameters, (b) H(t) vs time for the PVDF-HFP devices, (c) Arrhenius plot with ln(η) on the y-axis and 1/T in K in the x-axis, (d) Failure probability, F(t), as a function of time for pristine devices at V + 85 °C, 100 °C, 115 °C, and 130 °C. (e) F(t)-time curves for PVDF-HFP devices at the same temperatures. (f) Lifetime as a function of temperature for pristine and PVDF-HFP devices, summarizing the temperature dependence of device stability. The shaded regions represent the 80% confidence bands of the fitted lifetime-temperature trends.

becomes more uniform across the device population. This behavior is consistent with the stabilizing role of the PVDF-HFP additive, which likely improves interfacial and morphological uniformity, leading to enhanced operational reliability compared with pristine devices. Further, Fig. 8c shows the Arrhenius plot, plotted using the eq. (4)

$$\ln(\eta) = lnA + \frac{E_a}{K_B}\left(\frac{1}{T}\right) \quad (4)$$

η is the characteristic lifetime obtained using the Weibull distribution in Fig. 8a and b, A is a constant, E_a is the activation energy, K_B is the Boltzmann constant $= 8.617 \times 10^{-5} eV/K$, and T is the temperature in K. The Arrhenius slopes for the pristine and PVDF-HFP devices are 9665 and 11,035, corresponding to activation energies of 0.83 eV and 0.95 eV, respectively. The different activation energies indicate that the two devices follow different degradation pathways. The higher activation energy of the PVDF-HFP device means that more thermal energy is required for degradation to occur, suggesting that the polymer modifies the failure process compared to the pristine device. In particular, the strong interaction between the additive and the perovskite, such as Pb—F coordination, effectively increases the energy barrier for ion migration or interfacial degradation, thereby helping the device maintain structural integrity under thermal stress.

Further, using the Weibull parameters, F(t) was obtained and is plotted in Fig. 8d and e. For the lifetime evaluation, the 20% percentile is taken as the criterion for the minimum operational lifetime. The graphical method is used to predict the lifetime of the devices at room temperature (25 °C). Based on the fitted curves in Fig. 8d and Fig. 8e, the lifetime under each stress condition is extracted and plotted as a function of temperature in Fig. 8f. For both device types, as expected, the lifetime decreases with increasing temperature. However, at all temperatures, the PVDF-HFP devices exhibit systematically longer lifetimes than the pristine devices, confirming that polymer incorporation slows the dominant failure processes. Quantitatively, the lifetime advantage of PVDF-HFP is most pronounced at moderate high temperatures (≈85–100 °C), where the lifetime is extended by several hundred hours compared to pristine devices. As the temperature approaches 130 °C, the lifetimes of both device types converge to similarly low values, indicating that under extreme thermal stress the stabilizing effect of PVDF-HFP becomes insufficient, consistent with the rapid interfacial degradation observed in earlier sections. Notably, the slope of the fitted lines in Fig. 8f indicates that the acceleration factor for the pristine devices is −14.77 and for the PVDF-HFP devices is −23.83. According to this prediction, the lifetimes of the pristine devices and PVDF-HFP devices at 25 °C are expected to be 1444 and 2491 h, respectively. The corresponding 80% confidence intervals are estimated to be 493.3–2235.18 h for the pristine device and 1603.75–3345.64 h for the PVDF-HFP device. The relatively broad uncertainty bounds arise from the limited number of temperature-dependent lifetime data points and the extrapolation of accelerated-aging results to room temperature. Nevertheless, the PVDF-HFP devices show a higher estimated lifetime across the fitted confidence range. The Weibull-Arrhenius extrapolation assumes a similar dominant degradation pathway within the fitted temperature range.

After establishing the enhanced stability of the PVDF-HFP-modified devices under continuous thermal aging and confirming the reliability improvement through Weibull–Arrhenius lifetime analysis, thermal cycling measurements were performed to evaluate robustness under repeated temperature fluctuations. The devices were cycled between 130 and − 60 °C, with each temperature step maintained for 45 min, corresponding to a full cycle duration of approximately 90 min. As shown in Fig. 9a, the pristine device failed after approximately 8 cycles, whereas the PVDF-HFP-modified device still retained nearly 50% of its initial PCE after 10 cycles. The corresponding photovoltaic parameters in Fig. S14 (a-c) show concurrent losses in V_{oc}, J_{sc}, and FF, indicating that degradation arises from combined recombination, photocurrent-collection, and charge-extraction losses rather than a single parameter.

To further distinguish general thermal-cycling robustness from failure under extreme thermal shock, an additional cycling test was performed between 100 and − 60 °C using the same 45 min step duration and ~ 90 min full cycle. As shown in Fig. 9b, the pristine device retained only around 50% of its initial PCE after 10 cycles, whereas the PVDF-HFP-modified device maintained nearly its full initial PCE after 10 cycles. The corresponding parameter evolution in Fig. S14 (d-f) confirms that this improvement mainly arises from better retention of V_{oc} and FF. These results demonstrate that PVDF-HFP substantially improves thermal-cycling robustness, although its stabilizing effect becomes limited under the more extreme 130 ⇔ -60 °C condition. This limitation may be associated with the upper cycling temperature approaching the softening/melting region of PVDF-HFP, which can weaken the polymer-mediated interfacial stabilization during repeated thermal cycling.

Table 2 compares representative polymer-based stabilization strategies reported for PSCs with the present PVDF-HFP approach. Prior studies have mainly evaluated stability under ambient storage, humidity, or moderate thermal stress, whereas reports combining high-temperature operation with vacuum remain essentially absent. In contrast, our devices were examined under space-relevant vacuum + heat conditions over a broad temperature range, providing a more stringent assessment of operational reliability. This comparison highlights the distinct significance of the present work beyond conventional polymer-passivation studies.

3. Conclusion

This work evaluates the reliability of PVDF-HFP-modified p-i-n perovskite solar cells under space-relevant stress conditions, including

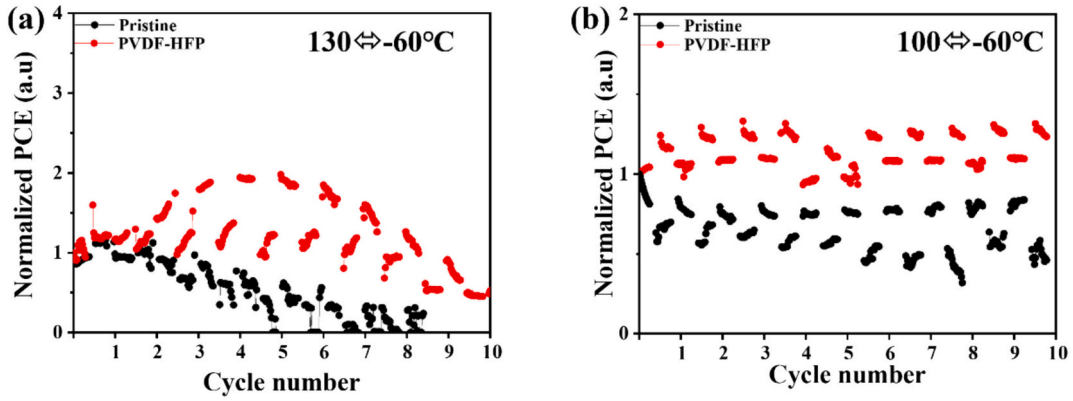

Fig. 9. Thermal cycling stability of pristine and PVDF-HFP-modified devices: normalized PCE retention during cycling between (a) 130 and − 60 °C and (b) 100 and − 60 °C, with a 90 min cycle duration.

Table 2
Comparison of representative polymer-based stabilization strategies reported for perovskite solar cells, categorized by polymer type, modified layer, testing condition, and stability metric.

Polymer	Modified layer	Testing condition	Stability result	Reference
PMMA	HTL (Spiro-OMeTAD)	Dark and RH = 35±5%	Over 90% after 100 days of storage	[62]
PMMA	Post-treatment passivation for perovskite	RH = 25–35% at 20–25 °C	95% of the initial PCE after 20 days	[63]
PEO	Perovskite bulk	RH ≈ 62.5±3.25%	~80% retained after 140 h	[64]
PEG	Passivation layer between perovskite and ETL	RH ~ 30% and 25 °C	~93% of initial PCE after 30 days	[65]
PVP	Additive in perovskite bulk and grain boundaries via confinement effect	85 °C in N_2 glove box	T_{80} is ~120 h	[66]
PVDF	Perovskite bulk	25±10°C, 50±10% RH in air	~90% PCE of initial PCE after 2500 h	[24]
PVDF-HFP	Perovskite bulk	10^{-3} Torr+heat (85 °C, 100 °C, 115 °C and 130 °C)	T_{80} is ~1200 h, ~500 h, ~200 h and ~ 50 h respectively	This work

Note: PMMA, poly(methyl methacrylate); PS, polystyrene; PEO, polyethylene oxide; PEG, polyethylene glycol; PVP, polyvinylpyrrolidone; PVDF, poly(vinylidene fluoride).

vacuum + light exposure and vacuum + thermal aging up to 130 °C. The optimized PVDF-HFP concentration improves device performance and stability by promoting defect passivation, preserving film morphology, and reducing recombination losses. Under vacuum + light stress, PVDF-HFP-modified devices show slower PCE degradation, smaller growth of non-radiative voltage loss, stronger PL/TRPL retention, lower Urbach-energy increase, and better preservation of the perovskite/PbI_2 ratio. These results indicate that PVDF-HFP suppresses illumination-assisted defect activation and delays phase degradation, leading to improved operational stability.

Under vacuum + thermal stress, PVDF-HFP significantly improves stability at 85–100 °C by suppressing PbI_2 formation, electronic disorder, carrier-lifetime loss, and morphological degradation. At higher temperatures, especially near 130 °C, degradation becomes increasingly governed by interfacial and transport-layer instability. The i-PCE and QFLS analyses identify the PVSK/PCBM junction as the most thermally vulnerable interface. In parallel, impedance spectroscopy shows that PVDF-HFP-modified devices retain higher R_{rec} after thermal stress, indicating suppressed recombination; at higher temperatures, the small tail observed in the Nyquist plots suggests additional slow interfacial/electrochemical processes.

Quantitative reliability analysis further supports these stability trends. Using a hazard-based Weibull framework combined with Arrhenius modeling, PVDF-HFP devices show longer characteristic lifetimes than pristine devices across all tested temperatures, with the largest improvement at moderately high temperatures of 85–100 °C. The higher activation energy of PVDF-HFP devices, 0.95 eV compared with 0.83 eV for pristine devices, indicates a modified thermally activated degradation pathway and a higher barrier for failure. Room-temperature lifetime extrapolation predicts longer operational lifetimes for PVDF-HFP devices, 2491 h compared with 1444 h for pristine devices. In addition, thermal cycling tests confirmed the improved dynamic thermal robustness of the PVDF-HFP-modified devices. The pristine device failed after ~8 cycles under 130 to −60 °C cycling, whereas the PVDF-HFP device retained nearly 50% PCE after 10 cycles; under 100 to −60 °C cycling, PVDF-HFP maintained nearly its initial PCE, while the pristine device retained only ~50%. These results confirm that PVDF-HFP extends device lifetime under practical thermal-stress conditions, while the convergence of lifetimes at 130 °C defines the operational limit of its stabilizing effect. Overall, PVDF-HFP enhances perovskite solar-cell stability and quantitatively extends device lifetime within realistic operating temperature windows, while clearly defining interfacial limitations under extreme thermal stress.

CRediT authorship contribution statement

Harini Srikanth Rao: Writing – original draft, Investigation. **Seoungjun Ahn:** Data curation. **Wei-Hao Chiu:** Writing – review & editing, Methodology. **Wei-Chen Chu:** Data curation. **Yi-Wen Sung:** Data curation. **Gao Chen:** Writing – review & editing, Methodology. **Kun-Mu Lee:** Writing – review & editing, Supervision.

Declaration of competing interest

The authors declare that they have no known competing financial interests or personal relationships that could have appeared to influence the work reported in this paper.

Acknowledgements

The authors thank the support from the National Science and Technology Council, Taiwan (Grant Number: 111-2223-E-182-001-MY4), Chang Gung University, Taoyuan, Taiwan (URRPD2R0011). During the preparation of this work, the authors used the free version of ChatGPT (developed by OpenAI) to improve the article's readability. The AI tool was not used to analyze the data. After using this tool, the authors reviewed and edited the content as needed and take full responsibility for the content of the published article.

Appendix A. Supplementary data

Supplementary data to this article can be found online at https://doi.org/10.1016/j.cej.2026.177494.

Data availability

Data will be made available on request.

References

[1] Artemis-NASA. https://www.nasa.gov/humans-in-space/artemis/, 2026. (Accessed 27 January 2026). April 10.
[2] Y. Tu, J. Wu, G. Xu, X. Yang, R. Cai, Q. Gong, R. Zhu, W. Huang, Perovskite solar cells for space applications: progress and challenges, Adv. Mater. 33 (21) (2021) 2006545.
[3] H.S. Rao, W.-H. Chiu, S.-H. Chen, M.-C. Wu, K.-M. Lee, Impact of proton radiation on the performance of single-junction perovskite solar cells for space applications, Sol. Energy Mater. Sol. Cells 295 (2026) 114015.
[4] Y. Zhou, Y. Yin, X. Zuo, L. Wang, T.-D. Li, Y. Xue, A. Subramanian, Y. Fang, Y. Guo, Z. Yang, Improving thermal stability of perovskite solar cells by suppressing ion migration using copolymer grain encapsulation, Chem. Mater. 33 (15) (2021) 6120–6135.
[5] A.C. Tribble, The Space Environment: Implications for Spacecraft Design, Revised and expanded edition, Princeton University Press, 2003.
[6] D.M. Fleetwood, Radiation effects in a post-Moore world, IEEE Trans. Nucl. Sci. 68 (5) (2021) 509–545.
[7] S. Wang, X.-Y. Gong, M.-X. Li, M.-H. Li, J.-S. Hu, Polymers for perovskite solar cells, JACS Au 4 (9) (2024) 3400–3412.
[8] M.H. Li, J.Y. Shao, Y. Jiang, F.Z. Qiu, S. Wang, J. Zhang, G. Han, J. Tang, F. Wang, Z. Wei, Electrical loss management by molecularly manipulating dopant-free poly (3-hexylthiophene) towards 16.93% CsPbI2Br solar cells, Angew. Chem. Int. Ed. Eng. 133 (30) (2021) 16524–16529.
[9] J. Chen, N.-G. Park, Materials and methods for interface engineering toward stable and efficient perovskite solar cells, ACS Energy Lett. 5 (8) (2020) 2742–2786.
[10] D. He, D. Ma, R. Li, B. Liu, Q. Zhou, H. Yang, S. Lu, Z. Zhang, C. Li, X. Li, Synergistically stabilizing hole transport layer and dual interface enables high-performance perovskite solar cells, ACS Energy Lett. 9 (6) (2024) 2615–2625.

[11] H. Wang, H. Liu, Z. Dong, W. Li, L. Zhu, H. Chen, Composition manipulation boosts the efficiency of carbon-based CsPbI3 perovskite solar cells to beyond 14%, Nano Energy 84 (2021) 105881.
[12] Y. An, N. Zhang, Z. Zeng, Y. Cai, W. Jiang, F. Qi, L. Ke, F.R. Lin, S.W. Tsang, T. Shi, Optimizing crystallization in wide-bandgap mixed halide perovskites for high-efficiency solar cells, Adv. Mater. 36 (17) (2024) 2306568.
[13] Y. Zhou, Y. Yin, X. Zuo, L. Wang, T.-D. Li, Y. Zhou, N.P. Padture, Z. Yang, Y. Guo, Y. Xue, Enhancing chemical stability and suppressing ion migration in CH3NH3PbI3 perovskite solar cells via direct backbone attachment of polyesters on grain boundaries, Chem. Mater. 32 (12) (2020) 5104–5117.
[14] Y. Chung, K.S. Kim, J.W. Jung, On the role of carboxylated polythiophene in defect passivation of CsPbI2Br surface for efficient and stable all-inorganic perovskite solar cells, Int. J. Energy Res. 46 (5) (2022) 6012–6021.
[15] C. Li, S. Tscheuschner, F. Paulus, P.E. Hopkinson, J. Kießling, A. Köhler, Y. Vaynzof, S. Huettner, Iodine migration and its effect on hysteresis in perovskite solar cells, Adv. Mater. 28 (12) (2016) 2446–2454.
[16] S. Meloni, T. Moehl, W. Tress, M. Franckevičius, M. Saliba, Y.H. Lee, P. Gao, M. K. Nazeeruddin, S.M. Zakeeruddin, U. Rothlisberger, Ionic polarization-induced current–voltage hysteresis in CH3NH3PbX3 perovskite solar cells, Nat. Commun. 7 (1) (2016) 10334.
[17] S. Zhang, Y. Lu, B. Lin, Y. Zhu, K. Zhang, N.-Y. Yuan, J.-N. Ding, B. Fang, PVDF-HFP additive for visible-light-semitransparent perovskite films yielding enhanced photovoltaic performance, Sol. Energy Mater. Sol. Cells 170 (2017) 178–186.
[18] Y. chi Zhang, M. qi Jin, Z. Zhou, K.Y. Huang, J.G. Yuan, Z.T. Shen, H.L. Li, Y. Liu, R. Liu, F.M. Li, Dual-functional PVDF-HFP additive inverted perovskite solar cells via defect passivation and hydrophobic protection, Mater. Today Chem. 50 (2025) 103157.
[19] B.A. Banks, J.A. Backus, M.V. Manno, D.L. Waters, K.C. Cameron, K.K. deGroh, Atomic oxygen erosion yield prediction for spacecraft polymers in low earth orbit, 11th International Symposium on Materials in a Space Environment (ISMSE), 2009.
[20] S. Ahn, W.-H. Chiu, W.-C. Chu, P.-Y. Chen, T.-H. Lin, K.-M. Lee, A systematic investigation of PVDF-HFP in perovskite solar cells for improved space mission reliability, Chem. Eng. J. 496 (2024) 153974.
[21] A.D. Sheikh, R. Munir, M.A. Haque, A. Bera, W. Hu, P. Shaikh, A. Amassian, T. Wu, Effects of high temperature and thermal cycling on the performance of perovskite solar cells: acceleration of charge recombination and deterioration of charge extraction, ACS Appl. Mater. Interfaces 9 (40) (2017) 35018–35029.
[22] F. Brivio, J.M. Frost, J.M. Skelton, A.J. Jackson, O.J. Weber, M.T. Weller, A. R. Goni, A.M. Leguy, P.R. Barnes, A. Walsh, Lattice dynamics and vibrational spectra of the orthorhombic, tetragonal, and cubic phases of methylammonium lead iodide, Phys. Rev. B 92 (14) (2015) 144308.
[23] I. Mesquita, L. Andrade, A. Mendes, Temperature impact on perovskite solar cells under operation, ChemSusChem 12 (10) (2019) 2186–2194.
[24] R. Sun, Q. Tian, M. Li, H. Wang, J. Chang, W. Xu, Z. Li, Y. Pan, F. Wang, T. Qin, Over 24% efficient poly (vinylidene fluoride)(PVDF)-coordinated perovskite solar cells with a photovoltage up to 1.22 V, Adv. Funct. Mater. 33 (6) (2023) 2210071.
[25] S. Narendhiran, A. Kunka Ravindran, I.D. Rajan Thomas, S.P. Muthu, R. Perumalsamy, Poly (vinylidene fluoride-co-hexafluoropropylene) additive in perovskite for stable performance of carbon-based perovskite solar cells, Int. J. Energy Res. 46 (2) (2022) 1565–1574.
[26] K. Daryabeigi, E. Kurz, Transient radiant thermal testing of reusable thermal protection systems and insulation materials, National Aeronautics and Space Administration, 2025.
[27] K. Almasabi, X. Zheng, B. Turedi, A.Y. Alsalloum, M.N. Lintangpradipto, J. Yin, L. Gutierrez-Arzaluz, K. Kotsovos, A. Jamal, I. Gereige, Hole-transporting self-assembled monolayer enables efficient single-crystal perovskite solar cells with enhanced stability, ACS Energy Lett. 8 (2) (2023) 950–956.
[28] C.A. Gueymard, D. Myers, K. Emery, Proposed reference irradiance spectra for solar energy systems testing, Sol. Energy 73 (6) (2002) 443–467.
[29] S. Haque, M. Alexandre, A.T. Vicente, K. Li, C.S. Schuster, S. Yang, H. Águas, R. Martins, R.A. Ferreira, M.J. Mendes, Photon shifting and trapping in perovskite solar cells for improved efficiency and stability, Light Sci. Appl. 13 (1) (2024) 238.
[30] X. Sun, Z. Li, X. Yu, X. Wu, C. Zhong, D. Liu, D. Lei, A.K.Y. Jen, Z.a. Li, Z. Zhu, Efficient inverted perovskite solar cells with low voltage loss achieved by a pyridine-based dopant-free polymer semiconductor, Angew. Chem. Int. Ed. 60 (13) (2021) 7227–7233.
[31] S. Valero, T. Soria, N. Marinova, J.L. Delgado, Efficient and stable perovskite solar cells based on perfluorinated polymers, Polym. Chem. 10 (42) (2019) 5726–5736.
[32] J. Huang, X. Li, Z. Zhang, T. Sun, H. Dong, H. Yu, X. Ma, W. Yang, L. Dai, L. Wang, Oriented crystallization of perovskite film via fluorine-containing Hyperbranched polymer for efficient and stable perovskite solar cells, Adv. Mater. 38 (2) (2026) e11684.
[33] E.T. Hoke, D.J. Slotcavage, E.R. Dohner, A.R. Bowring, H.I. Karunadasa, M. D. McGehee, Reversible photo-induced trap formation in mixed-halide hybrid perovskites for photovoltaics, Chem. Sci. 6 (1) (2015) 613–617.
[34] D. Bi, C. Yi, J. Luo, J.-D. Décoppet, F. Zhang, S.M. Zakeeruddin, X. Li, A. Hagfeldt, M. Grätzel, Polymer-templated nucleation and crystal growth of perovskite films for solar cells with efficiency greater than 21%, Nat. Energy 1 (10) (2016) 1–5.
[35] L. Zuo, H. Guo, D.W. deQuilettes, S. Jariwala, N. De Marco, S. Dong, R. DeBlock, D. S. Ginger, B. Dunn, M. Wang, Polymer-modified halide perovskite films for efficient and stable planar heterojunction solar cells, Sci. Adv. 3 (8) (2017) e1700106.
[36] J.A. Schwenzer, T. Hellmann, B.A. Nejand, H. Hu, T. Abzieher, F. Schackmar, I. M. Hossain, P. Fassl, T. Mayer, W. Jaegermann, Thermal stability and cation composition of hybrid organic–inorganic perovskites, ACS Appl. Mater. Interfaces 13 (13) (2021) 15292–15304.
[37] B. Conings, J. Drijkoningen, N. Gauquelin, A. Babayigit, J. D'Haen, L. D'Olieslaeger, A. Ethirajan, J. Verbeeck, J. Manca, E. Mosconi, Intrinsic thermal instability of methylammonium lead trihalide perovskite, Adv. Energy Mater. 5 (15) (2015) 1500477.
[38] B. Brunetti, C. Cavallo, A. Ciccioli, G. Gigli, A. Latini, On the thermal and thermodynamic (in) stability of methylammonium lead halide perovskites, Sci. Rep. 6 (1) (2016) 31896.
[39] B. Philippe, B.-W. Park, R. Lindblad, J. Oscarsson, S. Ahmadi, E.M. Johansson, H. Rensmo, Chemical and electronic structure characterization of Lead halide perovskites and stability behavior under different exposures a photoelectron spectroscopy investigation, Chem. Mater. 27 (5) (2015) 1720–1731.
[40] B. Ameduri, From vinylidene fluoride (VDF) to the applications of VDF-containing polymers and copolymers: recent developments and future trends, Chem. Rev. 109 (12) (2009) 6632–6686.
[41] X. He, K. Yao, B.K. Gan, Phase transition and properties of a ferroelectric poly (vinylidene fluoride-hexafluoropropylene) copolymer, J. Appl. Phys. 97 (8) (2005).
[42] T.S. Sherkar, C. Momblona, L. Gil-Escrig, J. Ávila, M. Sessolo, H.J. Bolink, L.J. A. Koster, Recombination in perovskite solar cells: significance of grain boundaries, interface traps, and defect ions, ACS Energy Lett. 2 (5) (2017) 1214–1222.
[43] T.T. Ava, A. Al Mamun, S. Marsillac, G. Namkoong, A review: thermal stability of methylammonium lead halide based perovskite solar cells, Appl. Sci. 9 (1) (2019) 188.
[44] S.M. Meroni, Y. Mouhamad, F. De Rossi, A. Pockett, J. Baker, R. Escalante, J. Searle, M.J. Carnie, E. Jewell, G. Oskam, Homogeneous and highly controlled deposition of low viscosity inks and application on fully printable perovskite solar cells, Sci. Technol. Adv. Mater. 19 (1) (2018) 1–9.
[45] E. Von Hauff, D. Klotz, Impedance spectroscopy for perovskite solar cells: characterisation, analysis, and diagnosis, J. Mater. Chem. C 10 (2) (2022) 742–761.
[46] J. Nie, B. Niu, Y. Wang, Z. He, X. Zhang, H. Zheng, Y. Lei, P. Zhong, X. Ma, Multi-functional MXene quantum dots enhance the quality of perovskite polycrystalline films and charge transport for solar cells, J. Colloid Interface Sci. 646 (2023) 517–528.
[47] J. Zhang, Z. Li, F. Guo, H. Jiang, W. Yan, C. Peng, R. Liu, L. Wang, H. Gao, S. Pang, Thermally crosslinked F-rich polymer to inhibit Lead leakage for sustainable perovskite solar cells and modules, Angew. Chem. Int. Ed. 62 (31) (2023) e202305221.
[48] K.-C. Hsiao, M.-H. Jao, K.-Y. Tian, T.-H. Lin, D.-P. Tran, H.-C. Liao, C.-H. Hou, J.-J. Shyue, M.-C. Wu, W.-F. Su, Acetamidinium cation to confer ion immobilization and structure stabilization of Organometal halide perovskite toward long life and high-efficiency p-i-n planar solar cell via air-Processable method, Sol. RRL 4 (9) (2020) 2000197.
[49] R. Segovia, G. Qu, M. Peng, X. Sun, H. Shi, B. Gao, Evolution of photoluminescence, Raman, and structure of CH3NH3PbI3 perovskite microwires under humidity exposure, Nanoscale Res. Lett. 13 (1) (2018) 79.
[50] Y. He, M.M. Islam, H. Tangara, M.A. Karim, M.E. Kayesh, T.H. Chowdhury, T. Sakurai, A. Islam, Study of the heat-induced degradation mechanism in PbI2-excess perovskite solar cells, Sol. RRL 7 (22) (2023) 2300580.
[51] V. Yeddu, K. Almasabi, Y. Xu, A. Amaro, S. Qiu, S. Dayneko, D. Zhang, P. Moazzezi, C. Tremblay, M.N. Lintangpradipto, In-situ self-assembly of hole transport monolayer during crystallization for efficient single-crystal perovskite solar cells, Nat. Commun. 16 (1) (2025) 7245.
[52] Z. Li, H.C. Wong, Z. Huang, H. Zhong, C.H. Tan, W.C. Tsoi, J.S. Kim, J.R. Durrant, J.T. Cabral, Performance enhancement of fullerene-based solar cells by light processing, Nat. Commun. 4 (1) (2013) 2227.
[53] T. Hahn, S. Tscheuschner, C. Saller, P. Strohriegl, P. Boregowda, T. Mukhopadhyay, S. Patil, D. Neher, H. Bässler, A. Köhler, Role of intrinsic photogeneration in single layer and bilayer solar cells with C60 and PCBM, J. Phys. Chem. C 120 (43) (2016) 25083–25091.
[54] G.J. Aalbers, T.P. van der Pol, K. Datta, W.H. Remmerswaal, M.M. Wienk, R. A. Janssen, Effect of sub-bandgap defects on radiative and non-radiative open-circuit voltage losses in perovskite solar cells, Nat. Commun. 15 (1) (2024) 1276.
[55] M. Abbas, X. Xu, M. Rauf, A.K.K. Kyaw, A comprehensive review on defects-induced voltage losses and strategies toward highly efficient and stable perovskite solar cells, Photonics (2024) 87. MDPI.
[56] H.-H. Huang, H. Tsai, R. Raja, S.-L. Lin, D. Ghosh, C.-H. Hou, J.-J. Shyue, S. Tretiak, W. Chen, K.-F. Lin, Robust unencapsulated perovskite solar cells protected by a fluorinated fullerene electron transporting layer, ACS Energy Lett. 6 (9) (2021) 3376–3385.
[57] H. Lee, C. Lee, Analysis of ion-diffusion-induced Interface degradation in inverted perovskite solar cells via restoration of the ag electrode, Adv. Energy Mater. 8 (11) (2018) 1702197.
[58] M. Li, R. Sun, J. Chang, J. Dong, Q. Tian, H. Wang, Z. Li, P. Yang, H. Shi, C. Yang, Orientated crystallization of FA-based perovskite via hydrogen-bonded polymer network for efficient and stable solar cells, Nat. Commun. 14 (1) (2023) 573.
[59] A.P. Morozov, L.O. Luchnikov, S.Y. Yurchuk, A.R. Ishteev, P.A. Gostishchev, S. I. Didenko, N.S. Saratovsky, S. Kozlov, D. Muratov, Y.N. Luponosov, Improvement of the perovskite photodiodes performance via advanced interface engineering with polymer dielectric, arXiv preprint 6 (2024) arXiv:2407.03260.
[60] E.A. Elsayed, Reliability Engineering, Third edition, 2020.
[61] C.M. Tan, Reliability Assessment of Integrated Circuits and its Misconception, in: Integrated Circuits, Photodiodes and Organic Field Effect Transistors, Nova Science Publishers, Inc., 2009, pp. 45–67.
[62] P. Xia, D.e. Guo, S. Lin, S. Liu, H. Huang, D. Kong, Y. Gao, W. Zhang, Y. Hu, C. Zhou, Simultaneous improvement of the power conversion efficiency and stability of perovskite solar cells by doping PMMA polymer in Spiro-OMeTAD-based hole-transporting layer, Sol. RRL 5 (11) (2021) 2100408.

[63] X. Zhang, Y. Zhou, Y. Li, J. Sun, X. Lu, X. Gao, J. Gao, L. Shui, S. Wu, J.-M. Liu, Efficient and carbon-based hole transport layer-free CsPbI 2 Br planar perovskite solar cells using PMMA modification, J. Mater. Chem. C 7 (13) (2019) 3852–3861.
[64] R.K. Koech, Y.A. Olanrewaju, R. Ichwani, M. Kigozi, D.O. Oyewole, O.V. Oyelade, D.M. Sanni, S.A. Adeniji, E. Colin-Ulloa, L.V. Titova, Effects of polyethylene oxide particles on the photo-physical properties and stability of FA-rich perovskite solar cells, Sci. Rep. 12 (1) (2022) 12860.
[65] X. Chen, Z. Wang, Z. Fan, H. Li, C. Zhang, S. Zheng, W. Zhu, Y. Wang, W. Sun, J. Wu, Polymer interface engineering for highly stable CsPbBr3 perovskite solar cells, Surf. Interfaces 73 (2025) 107503.
[66] S. Wu, S. Lin, Z. Shi, D.e. Guo, H. Huang, X. Zhou, D. Zhang, K. Zhou, W. Zhang, Y. Hu, Improved thermal stability and film uniformity of halide perovskite by confinement effect brought by polymer chains of polyvinyl pyrrolidone, Small 19 (25) (2023) 2207848.